

# Black hole mass accretion rates and efficiency factors for over 750 AGN and multiple GBH

Ruth A. Daly  1,2★

<sup>1</sup>*Pennsylvania State University, Berks Campus, Reading, PA 19608, USA*

<sup>2</sup>*Center for Computational Astrophysics, Flatiron Institute, 162 Fifth Avenue, New York, NY 10010, USA*

Accepted 2020 October 8. Received 2020 September 17; in original form 2020 July 24

## ABSTRACT

Mass accretion rates in dimensionless and physical units, and efficiency factors describing the total radiant luminosity of the disc and the beam power of the outflow are obtained and studied here for samples of black hole systems with outflows. Four samples of sources including 576 LINERs, 100 classical double (FR II) radio sources, 80 relatively local AGN, and 103 measurements of four stellar mass X-ray binary systems, referred to as Galactic Black Holes (GBHs), are included in the study. All of the sources have highly collimated outflows leading to compact radio emission or powerful extended (FR II) radio emission. The properties of each of the full samples are explored, as are those of the four individual GBH, and sub-types of the FR II and local AGN samples. Source types and sub-types that have high, medium, and low values of accretion rates and efficiency factors are identified and studied. A new efficiency factor that describes the relative impact of black hole spin and mass accretion rate on the beam power is defined and studied, and is found to provide a new and interesting diagnostic. Mass accretion rates for 13 sources and efficiency factors for 6 sources are compared with values obtained independently, and indicate that similar values are obtained with independent methods. The mass accretion rates and efficiency factors obtained here substantially increase the number of values available, and improve our understanding of their relationship to source types. The redshift dependence of quantities is presented and the impact on the results is discussed.

**Key words:** accretion, accretion discs – black hole physics – stars: black holes – galaxies: active – quasars: supermassive black holes.

## 1 INTRODUCTION

Mass accretion rates and associated efficiency factors are important quantities that describe the state of stellar and supermassive black hole systems. They provide information regarding processes that lead to the accretion, the state of the accretion disc, and how outflows and winds from accreting systems can affect their environment. Thus, they are important diagnostics of the state of the black hole system (e.g. Heckman & Best 2014; Yuan & Narayan 2014). Accretion rates and efficiency factors have been determined using a variety of methods and diagnostics, and this has allowed estimates of these quantities for sources with a broad range of properties (e.g. Bian & Zhao 2003; Davis & Laor 2011; Raimundo et al. 2012; Wu, Lu, & Zhang 2013; Trakhtenbrot 2014; Netzer & Trakhtenbrot 2014; Trakhtenbrot, Volonteri, & Natarajan 2014; Jiang et al. 2019; O’Dea & Saikia 2020).

Here, the new method of obtaining mass accretion rates introduced by Daly (2019) is applied to obtain and study accretion rates and efficiency factors. The ‘outflow method’ developed and applied by Daly (2016, 2019; hereafter D16 and D19) and Daly et al. (2018, hereafter D18) applies to black hole systems that include a black hole, accretion disc, and a highly collimated outflow. The highly collimated outflow must lead to radio emission from a compact radio source or from a powerful extended radio source that can be used to

study the properties of the highly collimated outflow, as described in Section 2. The method allows empirical determinations of accretion disc properties such as the mass accretion rate and disc magnetic field strength in dimensionless and physical units.

### 1.1 Overview of the outflow method

The outflow method of determining and studying black hole spin and accretion disc properties was proposed and applied by D16 and D19, and followed the methods developed and applied by Daly (2009, 2011) and Daly & Sprinkle (2014) to estimate black hole spin values based on outflow beam powers. A detailed overview of the method, its development, and its application is provided in section 1.1 of D19. The method is empirically based and includes one key theoretical input, as described below. To understand the method and its application, it is important to relinquish preconceived notions and assumptions that are based on the application of specific accretion disc or other models and focus on what is indicated empirically.

As is often the case with theoretical developments, with hindsight, simple arguments that are consistent with the original method become evident, even though this is not the way the method was developed or the results obtained. In this spirit, a heuristic path to understand the method and its application is described here. This provides an alternative path to arrive at the same conclusions even though this is not the way the equations were derived, which is explained in detail in section 1.1 of D19.

\* E-mail: rdaly@psu.edu

Consider a black hole with irreducible mass  $M$  and dimensionless spin parameter  $j$  that has an accretion disc accreting matter at a rate  $(dM/dt)$  in solar masses per year. A priori, these three quantities are independent. Given that the accretion disc of the system produces some bolometric luminosity,  $L_{\text{bol}}$ , the radiant efficiency of the disc may be determined empirically when  $\dot{M} \equiv (dM/dt)$  is known.

The outflow method has one key theoretical input, and the introduction of this theoretical input is motivated empirically. It is motivated by the fact that there are numerous black hole systems with outflow beam powers that exceed the bolometric luminosity of the disc by one to two orders of magnitude. For example, the results of D18 indicate that there are numerous black hole systems with beam powers that are 10–100 times larger than the bolometric luminosity of the accretion disc of the system (see fig. 2 of D18). In these cases, it is reasonable to suppose that the highly collimated outflow is powered at least in part by the black hole spin (see also Daly 2011; Narayan & McClintock 2012). D18 also showed that the slopes and normalizations of the relationship between  $\text{Log}(L_j/L_{\text{bol}})$  and  $\text{Log}(L_{\text{bol}}/L_{\text{Edd}})$  are consistent within uncertainties for the four samples studied, even though these quantities have a broad range of values of about  $(10^{-2}$  to  $10^2)$  for  $(L_j/L_{\text{bol}})$  and  $(10^{-6}$  to 1) for  $(L_{\text{bol}}/L_{\text{Edd}})$ , where  $L_j$  is the beam power and  $L_{\text{Edd}}$  is the Eddington luminosity. This suggests that the sources in the four samples studied by D18 are governed by the same physics, and therefore, all of the outflows are powered at least in part by black hole spin.

This indicates that the functional form of the theoretical equation that describes spin powered outflows (e.g. Blandford & Znajek 1977; Blandford 1990; Meier 1999) may be compared with the functional form of empirically determined relationships (D16; D18; D19). Once the theoretical equation is written in dimensionless separable form (see equation 1), terms in the empirically determined relationship may be identified with terms in the theoretical equation to solve for the properties of the accretion disc and black hole spin. Equation (1) is the primary theoretical input to the outflow method. Other aspects of the method are empirically based. No particular accretion disc emission model is assumed, and no detailed jet power/emission model is adopted.

D19 showed that the fundamental equation that describes outflows that are powered at least in part by black hole spin,  $L_j \propto B_p^2 M_{\text{dyn}}^2 f(j)$  (e.g. Blandford & Znajek 1977; Blandford 1990; Meier 1999) is separable and may be written as

$$(L_j/L_{\text{Edd}}) = g_j (B/B_{\text{Edd}})^2 F^2 \quad (1)$$

(see equation 6 from D19). Here,  $L_j$  is the beam power of the outflow, or the energy per unit time carried away from the black hole region in the form of a collimated outflow, typically thought to be in the form of directed kinetic energy,  $B_p$  is the poloidal component of the accretion disc magnetic field,  $B$  is the disc magnetic field strength,  $B_{\text{Edd}}$  is the Eddington magnetic field strength (e.g. Rees 1984; Blandford 1990; Dermer, Finke, & Menon 2008),  $B_{\text{Edd}} \approx 6(M_{\text{dyn}}/10^8 M_{\odot})^{-1/2} \times 10^4$  G,  $M_{\text{dyn}}$  is the total black hole mass, the normalized spin function is  $F^2 \equiv (f(j)/f_{\text{max}})$  where  $f(j)$  is the spin function and  $f_{\text{max}}$  is the maximum value of this function (see D19),  $g_j$  is the normalization factor for the beam power  $L_j$  in units of the Eddington Luminosity,  $L_{\text{Edd}}$ ,  $L_j/L_{\text{Edd}}(\text{max}) = g_j$ . It is clear that this is separable: information regarding the outflow is described by  $L_j/L_{\text{Edd}}$  and  $g_j$ ; that related to black hole spin is described by  $F^2$ ; and, as explained below, that related the accretion event is described by the term  $(B/B_{\text{Edd}})^2 = dm/dt = (L_{\text{bol}}/(g_{\text{bol}} L_{\text{Edd}}))^A$  (see equation 7 of D19), where the value of  $A$  is obtained for each sample from table 2 of D18, as summarized by D19, and is typically  $A \approx 0.45$ . Note that the ratio  $(B_p/B)^2$  is absorbed into the normalization factor

$g_j$ . The method was further developed and applied by D19 to study black hole spin functions and spin, the magnetic field strength of the accretion disc,  $B$  in physical units, and the magnetic field strength or pressure of the accretion disc in the dimensionless form  $(B/B_{\text{Edd}})$ . This work did not explicitly compute mass accretion rates in physical units or efficiency factors. These topics are addressed in this paper.

The identification of terms in equation (1) with empirically determined quantities was carried out with detailed calculations, presented and discussed by D16, D18, and D19. With hindsight a simple identification of terms becomes evident. The empirically determined relationship between beam power and disc luminosity, which by construction does not include a term related to black hole spin, has the form  $(L_j/L_{\text{Edd}}) \propto (L_{\text{bol}}/L_{\text{Edd}})^A$ , where the only term related to the overall properties of the accretion disc is  $(L_{\text{bol}}/L_{\text{Edd}})^A$ . In the theoretical equation given by equation (1) there is only one term that describes the overall properties of the accretion disc, and that is the term  $(B/B_{\text{Edd}})^2$ . Thus, identifying these terms, and noting that each is normalized to have a maximum value of unity, it is easy to see that

$$(B/B_{\text{Edd}})^2 = (L_{\text{bol}}/L_{\text{Edd}})^A, \quad (2)$$

as originally indicated by the detailed calculations discussed by D19.

To see how this is related to mass accretion rate, consider standard representations (e.g. Yuan & Narayan 2014; Ho 2009; D16) for the bolometric disc luminosity

$$L_{\text{bol}} \propto \epsilon_{\text{bol}} (dM/dt) \propto \epsilon_{\text{bol}} \dot{m} L_{\text{Edd}}, \quad (3)$$

and the beam power

$$L_j \propto (dM/dt) F^2 \propto \dot{m} L_{\text{Edd}} F^2, \quad (4)$$

where the efficiency factor  $\epsilon_{\text{bol}}$  that describes the radiant luminosity of the disc is not assumed to be constant, the dimensionless mass accretion rate is defined as  $\dot{m} \equiv \dot{M}/\dot{M}_{\text{Edd}}$ , and the Eddington mass accretion rate is defined as  $\dot{M}_{\text{Edd}} \equiv L_{\text{Edd}}/c^2$ . (Some authors adopt different definitions of the Eddington mass accretion rate and the dimensionless mass accretion rate. It is shown in Section 3.3 that consistent results are obtained with those definitions and the definitions adopted here.) Though equation (4) is most frequently adopted for sources with low values of  $(L_{\text{bol}}/L_{\text{Edd}})$ , it is reasonable to suppose that the same relationship holds for all of the sources since the samples studied include many sources with low values of  $(L_{\text{bol}}/L_{\text{Edd}})$ , and all of the samples have consistent values of the slope and normalization relating  $(L_j/L_{\text{Edd}})$  to  $(L_{\text{bol}}/L_{\text{Edd}})$  (e.g. D18). Combining equations (1), (2), (3), and (4), we obtain

$$\epsilon_{\text{bol}} = (dm/dt)^{(1-A)/A}, \quad (5)$$

where the constant of proportionality must be unity because  $\epsilon_{\text{bol}}$  and  $(dm/dt)$  are each normalized to have a maximum value of one. Thus,  $\epsilon_{\text{bol}} \simeq (dm/dt)^{1.2}$  or  $\epsilon_{\text{bol}} \simeq (dm/dt)$  for  $A \simeq 0.45$  and  $A \simeq 0.5$ , respectively (see also Ho 2009). Note that in D16, a more general functional form for  $L_j$  was adopted, and the same results were obtained. For the types of sources studied here,  $\epsilon_{\text{bol}}$  is only a constant when  $A = 1$ , which is quite clearly ruled out for these sources (D16, D18, D19). Substituting equation (3) into equation (2), and applying equation (5), we obtain

$$(B/B_{\text{Edd}})^2 = (\epsilon_{\text{bol}} \dot{m})^A = \dot{m}. \quad (6)$$

Thus,

$$dM/dt = \dot{m} L_{\text{Edd}} c^{-2} = (L_{\text{bol}}/L_{\text{Edd}})^A L_{\text{Edd}} c^{-2} \quad (7)$$

so  $dM/dt$  can be empirically determined using equation (7).

It is interesting to note that empirical results indicate  $(dm/dt)$  and thus  $\epsilon_{\text{bol}}$  are independent of the black hole spin function  $F$  and black hole spin (D16, D19). This is also suggested by the fact that there is no empirical indication that the relationship between  $(L_j/L_{\text{bol}})$  and  $(L_{\text{bol}}/L_{\text{Edd}})$  changes as  $(L_{\text{bol}}/L_{\text{Edd}}) \rightarrow 1$ , for the sources studied, as discussed by D16 and D19.

It is interesting to note that equation (2) provides an estimate of the gas pressure of the accretion disc in dimensionless form (see section 3.3 of D19). And the magnetic field strength of the disc, which is obtained from equation (2), provides an estimate of the disc pressure in physical units (see section 3.1 of D19).

Here, four samples of sources, including 756 AGN and 103 measurements of four stellar-mass black holes, associated with X-ray binaries are considered. The samples, source parameters, and parameter uncertainties are described in Section 2. Methods of obtaining mass accretion rates and efficiency factors are described in Sections 3.1 and 3.2, respectively. The results are discussed in Sections 4.1 and 4.2, respectively. An overview of the different source parameters associated with the accretion disc that can be obtained with the method, and the impact of the redshift range of the sources on the results are discussed in Section 5. The conclusions are summarized in Section 6.

## 2 DATA

Four samples are considered here. The samples include 576 LINERs from Nisbet & Best (2016) (hereafter NB16); 100 classical double (FRII) sources from D16 and D19; 80 local AGN that are compact radio sources from Merloni et al. (2003) (hereafter M03); and 103 observations of four stellar-mass Galactic Black Hole systems (GBH) that are in X-ray binary systems. The stellar-mass GBH data includes the 102 observations listed in table 2 of D19 plus one observation of A0 6200 discussed in section 5 of D19 (the data for the second observation of A0 6200 is from Gou et al. 2010; Kuulkers et al. 1999; and Owen et al. 1976). These are stellar mass X-ray binaries, and each of the GBH have multiple simultaneous radio and X-ray observations (Saikia et al. 2015, hereafter S15) who obtained the data from Corbel et al. (2013), Corbel, K rding, & Kaaret (2008), Zycki, Done & Smith (1999), Shahbaz et al. (1996), Merloni et al. (2003), Gallo et al. (2006), Gelino, Harrison & Orosz (2001), Shahbaz, Naylor & Charles (1994), and Jonker & Nelemans (2004). These four samples were studied by D19 who reported spin functions, spin values, and accretion disc magnetic field strengths in dimensionless and physical units for each source and observation.

The samples were selected for the purpose of studying black hole spin using source outflow properties following the work of Daly (2009, 2011), Narayan & McClintock (2012), and Daly & Sprinkle (2014), for example. It has long been thought that powerful collimated outflows from black hole systems are likely to be powered by black hole spin (e.g. Blandford & Znajek 1977; Rees 1984; Begelman, Blandford, & Rees 1984; Blandford 1990).

Individual samples, each comprised of a specific type of source including the NB16 LINERs, D16/D19 FRII (classical double) sources, M03 local AGN sample, and the S15 stellar-mass GBH were selected. The four different types of black hole systems allow studies of and comparisons between four different categories of black hole system, including supermassive and stellar-mass systems. Another criterion was that reliable determinations of the bolometric disc luminosity, beam power, and black hole mass were available.

The NB16 LINERs, M03 AGN, and S15 GBH all lie on the fundamental plane of black hole activity. Thus, black hole masses were available for all of the sources, bolometric disc luminosities

were obtained from the (2–10) keV X-ray luminosity using a standard conversion (e.g. Ho 2009; D18), and the beam powers were obtained by rotating the Fundamental Plane to the fundamental line of black hole activity using equation 4 of D18 and the values of C and D listed in table 1 of D18 for each sample. Note that time variability of the mass accretion rate and its impact on various source properties is discussed in detail in sections 5 and 6 of D19. For the FRII sources, the black hole masses were obtained from McLure et al. (2004, 2006). The bolometric disc luminosities were obtained from the O[III] luminosities of Grimes, Rawlings & Willott (2004) using a standard conversion (e.g. Heckman et al. 2004; Dicken et al. 2014). The beam powers were obtained using the strong shock method (described in detail in section 1.1 of D19) for 12 of the sources (O’Dea et al. 2009), and the relationship between beam power and 178 MHz radio luminosity obtained by Daly et al. (2012) using 31 sources with beam powers determined with the strong shock method (O’Dea et al. 2009). The source types are from Grimes, Rawlings & Willott (2004); W sources have weak emission lines, and Q sources are quasars.

Uncertainties of all quantities used to determine the black hole mass, bolometric luminosity, and beam power were included to obtain the uncertainty of each of these quantities, as described in section 2 of D19. The uncertainties  $\delta\text{Log}(L_{\text{Edd}})$ ,  $\delta\text{Log}(L_{\text{bol}})$ ,  $\delta\text{Log}(L_j)$  listed in section 2 of D19 are propagated to obtain uncertainties of all the quantities discussed in this paper using a method identical to that described in detail in section 3.3 of D19. For the GBH, the uncertainty of the black hole mass is small compared with uncertainties of the bolometric disc luminosity and the beam power, so uncertainties of the black hole mass are neglected for the GBH. In addition, the black hole mass of a given GBH is constant during the outflow events, and the black hole mass range for the GBH is small, so neither the dispersion of the GBH black hole mass nor the uncertainty of GBH black hole masses are included in Table 1.

Here, the dimensionless disc magnetic field strength, that is, the ratio of the accretion disc field strength to the Eddington magnetic field strength, is used to obtain the mass accretion rate in dimensionless and physical units for each system and for each observation of the GBH. The mass accretion rate of each source is combined with the bolometric disc luminosity, outflow beam power, and black hole spin function to define and study three efficiency factors associated with each black hole system, and the properties of different samples and types of sources are summarized in Table 1. Mass accretion rates and bolometric efficiency factors obtained here are compared with those obtained independently in Table 2. Results for individual sources and observations are listed in Tables 3–5 and 6 (online in supplementary material), and provide a measure of the state of the system at the time of the observation, since any given source may be time variable. Quantities are obtained in the context of a spatially flat cosmological model with mean mass density of non-relativistic matter relative to the critical density today of  $\Omega_m = 0.3$ , a similarly normalized cosmological constant of  $\Omega_\Lambda = 0.7$ , and a value of Hubble’s constant of  $70 \text{ km s}^{-1} \text{ Mpc}^{-1}$ .

## 3 METHOD

### 3.1 The mass accretion rate in dimensionless and physical units

The mass accretion rate of each source in dimensionless and physical units can be empirically determined, using the results obtained by D19 who showed that the dimensionless mass accretion rate  $(dm/dt) = (B/B_{\text{Edd}})^2$ , where  $B$  is the strength of the magnetic field anchored in the accretion disc and  $B_{\text{Edd}} \propto M_{\text{dyn}}^{-1/2}$  is the Eddington

**Table 1.** Mean value and dispersion of mass accretion rates and efficiency factors for each sample, sub-sample, or source; the estimated uncertainty per source of each quantity is indicated in (brackets) in the top part of the table.

(1)	(2)	(3)	(4)	(5)	(6)	(7)	(8)	(9)	(10)
Sample or source	Type	$N$	Log ( $dm/dt$ )	Log ( $dM/dt$ ) ( $M_{\odot} \text{ yr}^{-1}$ )	Log ( $\epsilon_{\text{bol}}$ )	Log ( $\epsilon_j$ )	Log ( $\epsilon_j/\epsilon_{\text{bol}}$ )	Log ( $\epsilon_{\text{std}}$ )	Log ( $M_{\text{dyn}}$ ) ( $M_{\odot}$ )
<b>NB16</b>	AGN-LIN	576	$-1.67 \pm 0.42(0.20)$	$-2.24 \pm 0.51(0.23)$	$-2.21 \pm 0.56(0.24)$	$-1.07 \pm 0.47(0.28)$	$1.14 \pm 0.73(0.31)$	$1.60 \pm 0.64(0.29)$	$8.07 \pm 0.50(0.35)$
<b>D16/D19</b>	AGN-FRII	100	$-0.38 \pm 0.34(0.24)$	$0.09 \pm 0.60(0.26)$	$-0.48 \pm 0.43(0.29)$	$-1.15 \pm 0.38(0.29)$	$-0.67 \pm 0.57(0.40)$	$0.23 \pm 0.51(0.37)$	$9.11 \pm 0.41(0.35)$
<b>M03</b>	AGN-Loc	80	$-1.17 \pm 0.84(0.26)$	$-1.97 \pm 0.99(0.30)$	$-1.68 \pm 1.22(0.32)$	$-1.33 \pm 0.71(0.38)$	$0.35 \pm 1.40(0.36)$	$0.83 \pm 1.10(0.35)$	$7.84 \pm 0.81(0.50)$
<b>S15</b>	GBH	103	$-0.74 \pm 0.46(0.12)$	$-8.56 \pm 0.45(0.12)$	$-0.84 \pm 0.52(0.15)$	$-1.34 \pm 0.18(0.14)$	$-0.51 \pm 0.56(0.28)$	$0.40 \pm 0.50(0.25)$	$0.83 \pm 0.09$
GX 339-4	GBH	76	$-0.65 \pm 0.36$	$-8.52 \pm 0.36$	$-0.74 \pm 0.40$	$-1.35 \pm 0.13$	$-0.61 \pm 0.41$	$0.31 \pm 0.37$	0.78
V404 Cyg	GBH	20	$-0.88 \pm 0.47$	$-8.53 \pm 0.47$	$-0.99 \pm 0.53$	$-1.20 \pm 0.12$	$-0.21 \pm 0.62$	$0.68 \pm 0.56$	1.00
J1118+480	GBH	5	$-1.08 \pm 0.02$	$-8.85 \pm 0.02$	$-1.22 \pm 0.04$	$-1.86 \pm 0.02$	$-0.63 \pm 0.06$	$0.23 \pm 0.04$	0.88
A0 6200	GBH	2	$-1.85 \pm 1.97$	$-9.68 \pm 1.97$	$-2.08 \pm 2.23$	$-1.21 \pm 0.05$	$0.88 \pm 2.28$	$1.66 \pm 2.01$	0.82
D16/19-AGN	W	3	$-0.16 \pm 0.31$	$-0.28 \pm 0.19$	$-0.20 \pm 0.39$	$-1.41 \pm 0.26$	$-1.21 \pm 0.36$	$-0.25 \pm 0.30$	$8.52 \pm 0.24(0.35)$
D16/19-AGN	Q	29	$-0.18 \pm 0.21$	$0.53 \pm 0.38$	$-0.23 \pm 0.27$	$-1.12 \pm 0.38$	$-0.88 \pm 0.42$	$0.07 \pm 0.40$	$9.36 \pm 0.46(0.40)$
D16/19-AGN	HEG	55	$-0.40 \pm 0.31$	$0.03 \pm 0.54$	$-0.51 \pm 0.40$	$-1.16 \pm 0.38$	$-0.65 \pm 0.58$	$0.24 \pm 0.52$	$9.07 \pm 0.33(0.35)$
D16/19-AGN	LEG	13	$-0.78 \pm 0.32$	$-0.58 \pm 0.52$	$-0.99 \pm 0.41$	$-1.14 \pm 0.37$	$-0.15 \pm 0.53$	$0.64 \pm 0.47$	$8.84 \pm 0.31(0.35)$
<b>M03-AGN</b>	NS1	7	$-0.24 \pm 0.31$	$-1.99 \pm 0.63$	$-0.35 \pm 0.45$	$-1.35 \pm 0.49$	$-1.00 \pm 0.61$	$-0.11 \pm 0.54$	$6.90 \pm 0.63(0.50)$
<b>M03-AGN</b>	Q	13	$-0.33 \pm 0.20$	$-0.85 \pm 0.46$	$-0.47 \pm 0.29$	$-1.50 \pm 0.91$	$-1.02 \pm 0.79$	$-0.17 \pm 0.82$	$8.13 \pm 0.42(0.50)$
<b>M03-AGN</b>	S(1-1.9)	17	$-0.89 \pm 0.66$	$-2.03 \pm 0.71$	$-1.27 \pm 0.95$	$-1.30 \pm 0.76$	$-0.03 \pm 1.07$	$0.58 \pm 0.89$	$7.50 \pm 0.46(0.50)$
<b>M03-AGN</b>	S2	22	$-1.27 \pm 0.54$	$-2.17 \pm 0.96$	$-1.83 \pm 0.77$	$-1.20 \pm 0.70$	$0.63 \pm 1.09$	$1.07 \pm 0.92$	$7.75 \pm 0.90(0.50)$
<b>M03-AGN</b>	L1.9	10	$-1.92 \pm 0.36$	$-2.19 \pm 0.71$	$-2.75 \pm 0.52$	$-1.34 \pm 0.66$	$1.41 \pm 0.85$	$1.57 \pm 0.76$	$8.37 \pm 0.66(0.50)$
<b>M03-AGN</b>	L2	10	$-2.09 \pm 0.40$	$-2.26 \pm 0.65$	$-3.00 \pm 0.58$	$-1.42 \pm 0.74$	$1.58 \pm 1.02$	$1.66 \pm 0.90$	$8.47 \pm 0.75(0.50)$

**Table 2.** Comparison of accretion rates and bolometric efficiency factors obtained here with independently determined values (see section 4).

(1) Source	(2) Type	(3) J19 ( $dm/dt$ )	(4) This work (T5) ( $dm/dt$ )	(5) Ratio (T5)/J19					
Ark 564	NS1	1.70	2.21	1.30					
Mrk 279	S1.5	0.75	0.48	0.64					
Mrk 335	NS1	0.74	0.51	0.69					
Mrk 590	S1.2	0.31	0.61	1.97					
PG 0804 + 761	Q	1.13	0.43	0.38					
PG 0844 + 349	Q	1.20	0.42	0.35					
PG 1229 + 204	Q	0.50	0.65	1.29					
PG 1426 + 015	Q	0.28	0.21	0.75					

(1) Source	(2) Type	(3) R12 (T1) ( $dM/dt$ ) ( $M_{\odot} \text{ yr}^{-1}$ )	(4) This work (T5) ( $dM/dt$ ) ( $M_{\odot} \text{ yr}^{-1}$ )	(5) Ratio (T5)/R12(T1)	(6) R12 (T3) $\epsilon_{\text{bol}}$	(7) This work (T5) $\epsilon_{\text{bol}}$	(8) Ratio (T5)/R12(T3)	(9) R12 (T2) $\epsilon_{\text{bol}}$	(10) Ratio (T5)/R12(T2)
Mrk 279	S1.5	0.045	0.045	1.00	0.25	0.35	1.40		
Mrk 509	NS1	0.095	0.082	0.86	0.29	0.37	1.28	0.46	0.80
NGC 5548	S1.5	0.006	0.067	11.64	0.98	0.16	0.16		
NGC 7469	S1	0.083	0.010	0.12	0.21	0.60	2.86	0.26	2.31
3C 120	S1	0.178	0.065	0.37	0.16	0.42	2.63		
3C 390.3	S1	0.062	0.202	3.28	0.36	0.15	0.42		

magnetic field strength (e.g. Rees 1984); D19 list empirically determined values of  $(B/B_{\text{Edd}})^2$  and  $B$  for each source. Given the definition of the dimensionless mass accretion rate,  $(dm/dt) \equiv (dM/dt)c^2/L_{\text{Edd}}$ , it is easy to see that

$$\left(\frac{dM}{dt}\right) = \left(\frac{B}{B_{\text{Edd}}}\right)^2 \left(\frac{L_{\text{Edd}}}{c^2}\right), \quad (8)$$

where  $L_{\text{Edd}}$  is the Eddington luminosity of the hole,  $L_{\text{Edd}} \simeq 1.3 \times 10^{38} (M_{\text{dyn}}/M_{\odot}) \text{ erg s}^{-1}$ , so the mass accretion rate in physical units  $dM/dt$  can be obtained from  $dm/dt$ . The results are summarized in Table 1.

A comparison between mass accretion rates obtained here with those obtained independently are discussed in Section 4.1 and are shown in Table 2.

Table 1 includes the mean value and dispersion of each quantity, with the dispersion measured by the  $1\sigma$  standard deviation of the sample or sub-sample. The uncertainty per source of each quantity is included in (brackets) following the mean value and dispersion of each quantity in the top part of Table 1. The uncertainty per source of each quantity is obtained by propagating the uncertainties  $\delta \text{Log}(L_{\text{bol}})$ ,  $\delta \text{Log}(L_j)$ ,  $\delta \text{Log}(L_{\text{Edd}})$  of the input parameters adopting a value of  $A \simeq 0.45$  for all samples, as described in Section 2.

### 3.2 Accretion disc and outflow efficiency factors

The efficiency factor of the accretion disc,  $\epsilon_{\text{bol}}$ , is defined as

$$\epsilon_{\text{bol}} \equiv \frac{L_{\text{bol}}}{(c^2 dM/dt)}. \quad (9)$$

For the sources studied here,  $L_{\text{bol}}$  is determined from the [O III] for the FRII sources, and from the (2–10) keV X-ray luminosity for the other samples (see D16 and D18), and the values of  $L_{\text{bol}}$  listed in Tables 2–5 from D19 are applied here. The mass accretion rate  $dM/dt$  is obtained as described in Sections 1.1 and 3.2.

A comparison between bolometric efficiency factor values,  $\epsilon_{\text{bol}}$ , obtained here with those obtained independently are discussed in Section 4.2 and are shown in Table 2.

The efficiency factor of the outflow,  $\epsilon_j$ , is defined as

$$\epsilon_j \equiv \frac{L_j}{(c^2 dM/dt)} = g_j F^2. \quad (10)$$

Outflow beam powers are based on the strong shock method for the FRII sources and on the mapping from the Fundamental Plane of black hole activity to the fundamental line of black hole activity for the three other samples, as described by D18 and D19 (see also O’Dea et al. 2009). The values of  $L_j$  listed in Tables 2–5 from D19 are applied here.

A new efficiency factor that measures the relative impact of black hole spin and the accretion disc on the Eddington-normalized beam power,  $\epsilon_{s/d}$ , is referred to as the ‘spin relative to disc’ efficiency factor. This efficiency factor is

$$\epsilon_{s/d} \equiv \frac{F^2}{(dm/dt)}. \quad (11)$$

This ratio is interesting because beam power in Eddington units may be written as,  $L_j/L_{\text{Edd}} = g_j(dm/dt)F^2$ , so the ratio  $F^2/(dm/dt) = g_j^{-1} (L_j/L_{\text{bol}}) (L_{\text{bol}}/L_{\text{Edd}})^{1-2A}$  measures the relative impact of black hole spin and the dimensionless mass accretion rate on the Eddington normalized outflow beam power (see equation 4).

The sample or sub-sample mean value and dispersion is listed in Table 1 for each quantity, and the uncertainty per source is included in brackets in top part of Table 1, as described in Section 2 and 3.1.

### 3.3 Comparison with other representations of key equations

Throughout these investigations, the total radiant luminosity of the accretion disc is represented in the standard form  $L_{\text{bol}} \propto \epsilon_{\text{bol}} \dot{M}$ , where the efficiency factor  $\epsilon_{\text{bol}}$  is not assumed to be constant (see Section 1.1). The dimensionless mass accretion rate and Eddington mass accretion rate are defined to be  $\dot{m} \equiv \dot{M}/\dot{M}_{\text{Edd}}$  and  $\dot{M}_{\text{Edd}} \equiv L_{\text{Edd}}/c^2$ , respectively.

An equivalent representation can be obtained by absorbing the efficiency factor into the definition of the Eddington mass accretion rate (e.g. Yuan & Narayan 2014). If the Eddington mass accretion

**Table 3.** Mass accretion rates and efficiency factors for stellar-mass galactic black holes (GBH) in X-ray binary systems.

(1)	(2)	(3)	(4)	(5)	(6)	(7)	(8)
Source	Log ( $dm/dt$ )	Log ( $dM/dt$ ) ( $M_{\odot} \text{ yr}^{-1}$ )	Log ( $\epsilon_{\text{bol}}$ )	Log ( $\epsilon_j$ )	Log ( $\epsilon_j/\epsilon_{\text{bol}}$ )	Log ( $\epsilon_{\text{sd}}$ )	Log ( $M_{\text{dyn}}$ ) ( $M_{\odot}$ )
GX 339-4	-0.38	-8.25	-0.45	-1.43	-0.98	-0.04	0.78
GX 339-4	-0.38	-8.25	-0.44	-1.43	-0.99	-0.04	0.78
GX 339-4	-0.58	-8.45	-0.67	-1.29	-0.62	0.30	0.78
GX 339-4	-0.66	-8.53	-0.72	-1.21	-0.49	0.44	0.78
GX 339-4	-0.92	-8.79	-1.03	-1.35	-0.32	0.56	0.78
GX 339-4	-0.68	-8.55	-0.77	-1.48	-0.71	0.20	0.78
GX 339-4	-0.40	-8.27	-0.47	-1.44	-0.97	-0.04	0.78
GX 339-4	-0.40	-8.27	-0.45	-1.43	-0.98	-0.04	0.78
GX 339-4	-0.74	-8.61	-0.82	-1.24	-0.42	0.50	0.78
GX 339-4	-0.76	-8.63	-0.85	-1.24	-0.39	0.52	0.78
GX 339-4	-0.56	-8.43	-0.62	-1.19	-0.57	0.36	0.78
GX 339-4	-0.92	-8.79	-1.05	-1.35	-0.30	0.58	0.78
GX 339-4	-0.32	-8.19	-0.36	-1.38	-1.02	-0.06	0.78
GX 339-4	-0.42	-8.29	-0.49	-1.34	-0.85	0.10	0.78
GX 339-4	-0.72	-8.59	-0.80	-1.37	-0.57	0.34	0.78
GX 339-4	-1.22	-9.09	-1.39	-1.17	0.22	1.06	0.78
GX 339-4	-0.50	-8.37	-0.55	-1.32	-0.77	0.18	0.78
GX 339-4	-0.82	-8.69	-0.94	-1.46	-0.52	0.36	0.78
GX 339-4	-0.88	-8.75	-1.00	-1.44	-0.44	0.44	0.78
GX 339-4	-1.02	-8.89	-1.15	-1.45	-0.30	0.58	0.78
GX 339-4	-0.88	-8.75	-1.01	-1.43	-0.42	0.46	0.78
GX 339-4	-0.98	-8.85	-1.11	-1.76	-0.65	0.22	0.78
GX 339-4	-1.14	-9.01	-1.31	-1.36	-0.05	0.80	0.78
GX 339-4	-1.24	-9.11	-1.38	-1.26	0.12	0.98	0.78
GX 339-4	-1.00	-8.87	-1.13	-1.31	-0.18	0.68	0.78
GX 339-4	-1.02	-8.89	-1.14	-1.29	-0.15	0.74	0.78
GX 339-4	-1.10	-8.97	-1.23	-1.64	-0.41	0.46	0.78
GX 339-4	-1.26	-9.13	-1.42	-1.13	0.29	1.14	0.78
GX 339-4	-0.72	-8.59	-0.79	-1.28	-0.49	0.44	0.78
GX 339-4	-0.78	-8.65	-0.86	-1.25	-0.39	0.52	0.78
GX 339-4	-0.70	-8.57	-0.80	-1.17	-0.37	0.54	0.78
GX 339-4	-0.86	-8.73	-0.98	-1.37	-0.39	0.50	0.78
GX 339-4	-0.82	-8.69	-0.91	-1.32	-0.41	0.48	0.78
GX 339-4	-0.82	-8.69	-0.94	-1.35	-0.41	0.48	0.78
GX 339-4	-0.76	-8.63	-0.87	-1.28	-0.41	0.48	0.78
GX 339-4	-0.04	-7.91	-0.03	-1.31	-1.28	-0.28	0.78
GX 339-4	-0.04	-7.91	-0.05	-1.34	-1.29	-0.30	0.78
GX 339-4	-1.16	-9.03	-1.32	-1.51	-0.19	0.66	0.78
GX 339-4	-0.92	-8.79	-1.04	-1.40	-0.36	0.52	0.78
GX 339-4	-0.28	-8.15	-0.33	-1.35	-1.02	-0.06	0.78
GX 339-4	-0.28	-8.15	-0.33	-1.38	-1.05	-0.10	0.78
GX 339-4	-0.24	-8.11	-0.28	-1.35	-1.07	-0.10	0.78
GX 339-4	-0.22	-8.09	-0.27	-1.35	-1.08	-0.12	0.78
GX 339-4	-0.18	-8.05	-0.20	-1.32	-1.12	-0.14	0.78
GX 339-4	-0.14	-8.01	-0.17	-1.32	-1.15	-0.18	0.78
GX 339-4	-0.12	-7.99	-0.13	-1.26	-1.13	-0.14	0.78
GX 339-4	-0.10	-7.97	-0.12	-1.23	-1.11	-0.14	0.78
GX 339-4	-0.10	-7.97	-0.09	-1.24	-1.15	-0.16	0.78
GX 339-4	-0.08	-7.95	-0.10	-1.31	-1.21	-0.22	0.78
GX 339-4	-0.56	-8.43	-0.62	-1.28	-0.66	0.28	0.78
GX 339-4	-0.22	-8.09	-0.25	-1.51	-1.26	-0.28	0.78
GX 339-4	-0.04	-7.91	-0.05	-1.47	-1.42	-0.42	0.78
GX 339-4	-0.16	-8.03	-0.18	-1.50	-1.32	-0.34	0.78
GX 339-4	-1.20	-9.07	-1.36	-1.31	0.05	0.90	0.78
GX 339-4	-1.12	-8.99	-1.27	-1.34	-0.07	0.78	0.78
GX 339-4	-0.92	-8.79	-1.05	-1.51	-0.46	0.42	0.78
GX 339-4	-1.14	-9.01	-1.29	-1.40	-0.11	0.74	0.78
GX 339-4	-1.14	-9.01	-1.29	-1.38	-0.09	0.76	0.78
GX 339-4	-0.68	-8.55	-0.75	-1.39	-0.64	0.28	0.78

Table 3 – continued

(1)	(2)	(3)	(4)	(5)	(6)	(7)	(8)
Source	Log ( $dm/dt$ )	Log ( $dM/dt$ ) ( $M_{\odot} \text{ yr}^{-1}$ )	Log ( $\epsilon_{\text{bol}}$ )	Log ( $\epsilon_j$ )	Log ( $\epsilon_j/\epsilon_{\text{bol}}$ )	Log ( $\epsilon_{\text{std}}$ )	Log ( $M_{\text{dyn}}$ ) ( $M_{\odot}$ )
GX 339–4	–0.60	–8.47	–0.66	–1.36	–0.70	0.24	0.78
GX 339–4	–0.80	–8.67	–0.90	–1.37	–0.47	0.42	0.78
GX 339–4	–0.74	–8.61	–0.83	–1.43	–0.60	0.30	0.78
GX 339–4	–0.80	–8.67	–0.92	–1.36	–0.44	0.44	0.78
GX 339–4	–0.82	–8.69	–0.91	–1.36	–0.45	0.46	0.78
GX 339–4	–0.56	–8.43	–0.63	–1.20	–0.57	0.36	0.78
GX 339–4	–1.04	–8.91	–1.19	–1.94	–0.75	0.10	0.78
GX 339–4	–0.86	–8.73	–0.98	–1.18	–0.20	0.68	0.78
GX 339–4	–0.78	–8.65	–0.90	–1.18	–0.28	0.62	0.78
GX 339–4	–0.72	–8.59	–0.80	–1.19	–0.39	0.52	0.78
GX 339–4	–0.66	–8.53	–0.75	–1.23	–0.48	0.44	0.78
GX 339–4	–0.62	–8.49	–0.70	–1.24	–0.54	0.38	0.78
GX 339–4	–0.06	–7.93	–0.08	–1.29	–1.21	–0.24	0.78
GX 339–4	–0.08	–7.95	–0.09	–1.28	–1.19	–0.20	0.78
GX 339–4	–0.08	–7.95	–0.10	–1.27	–1.17	–0.18	0.78
GX 339–4	–0.96	–8.83	–1.08	–1.30	–0.22	0.66	0.78
GX 339–4	–0.92	–8.79	–1.03	–1.24	–0.21	0.66	0.78
XTE J1118+480	–1.06	–8.83	–1.18	–1.88	–0.70	0.18	0.88
XTE J1118+480	–1.10	–8.87	–1.25	–1.84	–0.59	0.26	0.88
XTE J1118+480	–1.10	–8.87	–1.24	–1.84	–0.60	0.26	0.88
XTE J1118+480	–1.10	–8.87	–1.26	–1.84	–0.58	0.26	0.88
XTE J1118+480	–1.06	–8.83	–1.19	–1.88	–0.69	0.18	0.88
V404 Cyg	–0.54	–8.19	–0.60	–1.29	–0.69	0.24	1.00
V404 Cyg	–2.60	–10.25	–2.92	–0.86	2.06	2.74	1.00
V404 Cyg	–0.54	–8.19	–0.61	–1.28	–0.67	0.26	1.00
V404 Cyg	–0.70	–8.35	–0.79	–1.34	–0.55	0.36	1.00
V404 Cyg	–0.58	–8.23	–0.65	–1.12	–0.47	0.46	1.00
V404 Cyg	–0.90	–8.55	–1.02	–1.29	–0.27	0.62	1.00
V404 Cyg	–0.58	–8.23	–0.66	–1.08	–0.42	0.50	1.00
V404 Cyg	–1.24	–8.89	–1.40	–1.11	0.29	1.14	1.00
V404 Cyg	–0.88	–8.53	–0.98	–1.25	–0.27	0.62	1.00
V404 Cyg	–0.90	–8.55	–1.02	–1.27	–0.25	0.64	1.00
V404 Cyg	–0.66	–8.31	–0.73	–1.33	–0.60	0.32	1.00
V404 Cyg	–0.78	–8.43	–0.88	–1.19	–0.31	0.60	1.00
V404 Cyg	–0.94	–8.59	–1.07	–1.25	–0.18	0.70	1.00
V404 Cyg	–0.88	–8.53	–1.00	–1.30	–0.30	0.58	1.00
V404 Cyg	–0.56	–8.21	–0.62	–1.27	–0.65	0.28	1.00
V404 Cyg	–0.44	–8.09	–0.49	–1.15	–0.66	0.28	1.00
V404 Cyg	–1.30	–8.95	–1.46	–1.14	0.32	1.16	1.00
V404 Cyg	–1.18	–8.83	–1.33	–1.10	0.23	1.08	1.00
V404 Cyg	–0.82	–8.47	–0.92	–1.26	–0.34	0.56	1.00
V404 Cyg	–0.56	–8.21	–0.61	–1.13	–0.52	0.42	1.00
A0 6200	–3.24	–11.07	–3.66	–1.17	2.49	3.08	0.82
A0 6200	–0.46	–8.29	–0.50	–1.24	–0.74	0.24	0.82

rate is defined as  $\dot{M}'_{\text{Edd}} \equiv L_{\text{Edd}}/(\epsilon_{\text{bol}}c^2)$ , and the dimensionless mass accretion rate is defined as  $\dot{m}' \equiv \dot{M}/\dot{M}'_{\text{Edd}}$ , then  $L_{\text{bol}}$  becomes  $L_{\text{bol}} \propto \dot{m}' M_{\text{dyn}}$ , with  $\dot{m}' = \epsilon_{\text{bol}}\dot{m}$ .

Since both **D16** and **D19** empirically determined that the efficiency factor  $\epsilon_{\text{bol}}$  cannot be constant for the sources studied, the first representation given by equation (3), which allows explicit tracking of this efficiency factor, was selected.

## 4 RESULTS

Mass accretion rates in dimensionless and physical units obtained as described in Section 3.1 and efficiency factors obtained as described in Section 3.2 are summarized in Table 1. The mean value and dispersion (i.e. the one sigma standard deviation) for the sample,

sub-sample, or source listed in column (1) are provided for each quantity. The estimated uncertainty per source of each quantity is indicated in brackets following the mean value and dispersion in the top part of the table, obtained as described in Section 2 and 3.1. The input values used to compute each quantity are obtained from **D19**; for completeness, black hole mass is included in the Tables presented here.

A comparison of mass accretion rates and bolometric efficiency factors obtained independently is provided in Table 2.

Mass accretion rates, efficiency factors, and black hole masses for each source and measurement for the **S15** sample of GBH, the **D16/D19** sample of classical double (FR II) sources, the **M03** sample of local AGN, and the **NB16** sample of LINERs are listed in Tables 3, 4, 5, and 6 (online in supplementary material), respectively.

**Table 4.** Mass accretion rates and efficiency factors for the D16/D19 classical double (FR II) sources.

(1)	(2)	(3)	(4)	(5)	(6)	(7)	(8)	(9)	(10)
Source	Type	$z$	Log ( $dm/dt$ )	Log ( $dM/dt$ ) ( $M_{\odot} \text{ yr}^{-1}$ )	Log ( $\epsilon_{\text{bol}}$ )	Log ( $\epsilon_j$ )	Log ( $\epsilon_j/\epsilon_{\text{bol}}$ )	Log ( $\epsilon_{\text{slr}}$ )	Log ( $M_{\text{dyn}}$ ) ( $M_{\odot}$ )
3C 33	HEG	0.059	-0.46	-0.54	-0.58	-1.83	-1.25	-0.37	8.56
3C 192	HEG	0.059	-0.57	-0.81	-0.73	-1.90	-1.17	-0.33	8.41
3C 285	HEG	0.079	-1.00	-1.12	-1.28	-1.60	-0.32	0.40	8.53
3C 452	HEG	0.081	-0.77	-0.70	-0.98	-1.44	-0.47	0.32	8.71
3C 388	HEG	0.09	-1.24	-1.05	-1.58	-1.30	0.28	0.94	8.84
3C 321	HEG	0.096	-0.49	-0.35	-0.62	-2.18	-1.56	-0.69	8.78
3C 433	HEG	0.101	-1.18	-0.87	-1.51	-1.09	0.42	1.09	8.96
3C 20	HEG	0.174	-0.85	-0.92	-1.08	-0.73	0.36	1.13	8.58
3C 28	HEG	0.195	-0.65	-0.42	-0.83	-1.46	-0.63	0.19	8.87
3C 349	HEG	0.205	-0.69	-0.78	-0.88	-1.16	-0.28	0.53	8.56
3C 436	HEG	0.214	-0.77	-0.57	-0.99	-1.22	-0.23	0.56	8.85
3C 171	HEG	0.238	-0.23	-0.28	-0.29	-1.39	-1.10	-0.16	8.60
3C 284	HEG	0.239	-0.49	-0.25	-0.63	-1.61	-0.98	-0.11	8.89
3C 300	HEG	0.27	-0.35	-0.44	-0.45	-1.16	-0.70	0.20	8.56
3C 438	HEG	0.29	-0.91	-0.45	-1.16	-0.76	0.41	1.16	9.11
3C 299	HEG	0.367	-0.08	-0.15	-0.10	-1.37	-1.26	-0.29	8.57
3C 42	HEG	0.395	-0.65	-0.35	-0.82	-1.09	-0.27	0.56	8.94
3C 16	HEG	0.405	-0.56	-0.54	-0.71	-0.88	-0.17	0.68	8.66
3C 274.1	HEG	0.422	-0.94	-0.65	-1.20	-0.60	0.60	1.34	8.93
3C 457	HEG	0.428	-0.39	-0.23	-0.49	-1.08	-0.58	0.31	8.80
3C 244.1	HEG	0.428	-0.23	0.11	-0.29	-1.73	-1.44	-0.50	8.98
3C 46	HEG	0.437	-0.42	0.12	-0.54	-1.49	-0.95	-0.07	9.19
3C 341	HEG	0.448	-0.35	0.03	-0.44	-1.39	-0.95	-0.04	9.02
3C 172	HEG	0.519	-0.17	0.08	-0.21	-1.35	-1.14	-0.18	8.89
3C 330	HEG	0.549	-0.05	0.42	-0.06	-1.28	-1.21	-0.23	9.11
3C 49	HEG	0.621	-0.39	0.07	-0.50	-1.21	-0.71	0.18	9.11
3C 337	HEG	0.635	-0.78	-0.46	-0.99	-0.99	0.00	0.79	8.96
3C 34	HEG	0.69	0.12	0.69	0.15	-1.64	-1.79	-0.76	9.21
3C 441	HEG	0.708	-0.50	0.10	-0.64	-1.05	-0.41	0.45	9.24
3C 247	HEG	0.749	-0.27	0.49	-0.35	-1.71	-1.36	-0.44	9.41
3C 277.2	HEG	0.766	-0.01	0.39	-0.01	-1.22	-1.21	-0.21	9.04
3C 340	HEG	0.775	-0.28	0.11	-0.36	-1.05	-0.69	0.23	9.04
3C 352	HEG	0.806	-0.05	0.51	-0.06	-1.34	-1.28	-0.30	9.20
3C 263.1	HEG	0.824	-0.23	0.39	-0.30	-1.04	-0.74	0.19	9.27
3C 217	HEG	0.897	-0.05	0.12	-0.07	-0.89	-0.82	0.16	8.82
3C 175.1	HEG	0.92	-0.31	0.14	-0.39	-0.85	-0.46	0.46	9.09
3C 289	HEG	0.967	-0.68	0.11	-0.86	-0.94	-0.08	0.74	9.43
3C 280	HEG	0.996	0.06	0.85	0.08	-1.88	-1.96	-0.94	9.43
3C 356	HEG	1.079	-0.32	0.48	-0.41	-0.83	-0.42	0.49	9.45
3C 252	HEG	1.103	-0.11	0.54	-0.15	-1.07	-0.93	0.04	9.30
3C 368	HEG	1.132	-0.15	0.66	-0.19	-1.03	-0.84	0.12	9.45
3C 267	HEG	1.14	-0.25	0.49	-0.32	-0.97	-0.65	0.28	9.39
3C 324	HEG	1.206	-0.25	0.67	-0.32	-1.24	-0.92	0.01	9.56
3C 266	HEG	1.275	0.03	0.75	0.03	-1.16	-1.19	-0.19	9.37
3C 13	HEG	1.351	-0.21	0.74	-0.27	-1.09	-0.83	0.12	9.60
4C 13.66	HEG	1.45	-0.06	0.49	-0.08	-0.84	-0.77	0.22	9.20
3C 437	HEG	1.48	-0.26	0.48	-0.33	-0.38	-0.05	0.88	9.38
3C 241	HEG	1.617	-0.17	0.75	-0.22	-0.95	-0.73	0.22	9.57
3C 470	HEG	1.653	-0.48	0.32	-0.61	-0.61	-0.01	0.86	9.44
3C 322	HEG	1.681	-0.49	0.38	-0.62	-0.43	0.19	1.06	9.51
3C 239	HEG	1.781	-0.33	0.59	-0.42	-0.66	-0.24	0.67	9.57
3C 294	HEG	1.786	-0.03	0.79	-0.03	-0.90	-0.87	0.13	9.46
3C 225B	HEG	0.582	-0.29	0.06	-0.38	-0.94	-0.56	0.36	9.00
3C 55	HEG	0.735	-0.50	0.01	-0.64	-0.52	0.12	0.98	9.16
3C 68.2	HEG	1.575	-0.25	0.65	-0.31	-1.09	-0.77	0.16	9.54
3C 35	LEG	0.067	-1.37	-1.36	-1.74	-1.51	0.23	0.86	8.65
3C 326	LEG	0.088	-0.97	-1.24	-1.24	-1.18	0.06	0.79	8.38
3C 236	LEG	0.099	-1.24	-1.07	-1.57	-1.41	0.17	0.83	8.81
4C 12.03	LEG	0.156	-1.08	-0.87	-1.37	-1.37	0.00	0.70	8.85

Table 4 – continued

(1)	(2)	(3)	(4)	(5)	(6)	(7)	(8)	(9)	(10)
Source	Type	$z$	Log ( $dm/dt$ )	Log ( $dM/dt$ ) ( $M_{\odot} \text{ yr}^{-1}$ )	Log ( $\epsilon_{\text{bol}}$ )	Log ( $\epsilon_j$ )	Log ( $\epsilon_j/\epsilon_{\text{bol}}$ )	Log ( $\epsilon_{sl}$ )	Log ( $M_{\text{dyn}}$ ) ( $M_{\odot}$ )
3C 319	LEG	0.192	-0.81	-1.13	-1.03	-0.79	0.24	1.02	8.32
3C 132	LEG	0.214	-0.64	-0.55	-0.82	-1.35	-0.53	0.29	8.74
3C 123	LEG	0.218	-0.73	-0.56	-0.93	-0.37	0.56	1.36	8.82
3C 153	LEG	0.277	-0.52	-0.23	-0.66	-1.42	-0.76	0.10	8.94
4C 14.27	LEG	0.392	-0.61	-0.52	-0.77	-0.93	-0.16	0.67	8.73
3C 200	LEG	0.458	-0.45	-0.15	-0.57	-1.18	-0.60	0.27	8.94
3C 295	LEG	0.461	-0.90	-0.08	-1.14	-0.54	0.60	1.35	9.46
3C 19	LEG	0.482	-0.53	-0.01	-0.67	-1.28	-0.60	0.25	9.16
3C 427.1	LEG	0.572	-0.29	0.23	-0.37	-1.49	-1.12	-0.20	9.16
3C 249.1	Q	0.311	-0.22	0.44	-0.27	-2.11	-1.84	-0.90	9.30
3C 351	Q	0.371	-0.54	0.31	-0.69	-1.76	-1.07	-0.22	9.50
3C 215	Q	0.411	-0.12	-0.47	-0.16	-0.92	-0.76	0.20	8.30
3C 47	Q	0.425	-0.22	0.34	-0.27	-1.41	-1.13	-0.19	9.20
3C 334	Q	0.555	-0.40	0.66	-0.50	-1.62	-1.12	-0.23	9.70
3C 275.1	Q	0.557	0.04	-0.30	0.05	-1.51	-1.56	-0.55	8.30
3C 263	Q	0.646	0.02	0.47	0.02	-1.40	-1.42	-0.41	9.10
3C 207	Q	0.684	-0.01	-0.15	-0.01	-0.76	-0.75	0.25	8.50
3C 254	Q	0.734	-0.07	0.59	-0.09	-1.54	-1.45	-0.47	9.30
3C 175	Q	0.768	-0.60	0.65	-0.77	-1.30	-0.54	0.30	9.90
3C 196	Q	0.871	-0.48	0.48	-0.61	-0.62	-0.01	0.86	9.60
3C 309.1	Q	0.904	0.01	0.47	0.02	-1.04	-1.05	-0.05	9.10
3C 336	Q	0.927	-0.14	0.42	-0.17	-1.16	-0.99	-0.03	9.20
3C 245	Q	1.029	-0.20	0.55	-0.26	-1.12	-0.86	0.09	9.40
3C 212	Q	1.049	-0.13	0.43	-0.16	-0.92	-0.76	0.21	9.20
3C 186	Q	1.063	-0.10	0.75	-0.13	-1.20	-1.07	-0.10	9.50
3C 208	Q	1.11	-0.22	0.53	-0.29	-0.93	-0.64	0.30	9.40
3C 204	Q	1.112	-0.38	0.47	-0.49	-1.00	-0.52	0.38	9.50
3C 190	Q	1.197	0.18	0.23	0.22	-0.61	-0.83	0.22	8.70
3C 68.1	Q	1.238	-0.51	0.75	-0.65	-0.89	-0.24	0.62	9.90
4C 16.49	Q	1.296	-0.46	0.69	-0.59	-1.11	-0.52	0.35	9.80
3C 181	Q	1.382	0.09	1.04	0.11	-1.29	-1.40	-0.37	9.60
3C 268.4	Q	1.4	-0.05	1.10	-0.07	-0.94	-0.87	0.11	9.80
3C 14	Q	1.469	-0.04	0.72	-0.05	-1.09	-1.04	-0.05	9.40
3C 270.1	Q	1.519	-0.03	0.33	-0.03	-0.19	-0.15	0.84	9.00
3C 205	Q	1.534	-0.07	0.88	-0.10	-1.12	-1.03	-0.05	9.60
3C 432	Q	1.805	-0.44	1.02	-0.55	-1.13	-0.58	0.30	10.10
3C 191	Q	1.956	-0.03	1.03	-0.03	-1.01	-0.98	0.02	9.70
3C 9	Q	2.012	-0.23	0.93	-0.29	-0.71	-0.42	0.52	9.80
3C 223	W	0.136	-0.34	-0.50	-0.43	-1.71	-1.28	-0.37	8.48
3C 79	W	0.255	-0.33	-0.20	-0.43	-1.25	-0.82	0.09	8.78
3C 109	W	0.305	0.20	-0.15	0.25	-1.28	-1.54	-0.48	8.30

#### 4.1 Mass accretion rates

Histograms of mass accretion rates in dimensionless and physical units are shown in Figs 1 and 2. The mean value and  $1\sigma$  dispersion of each sample is listed in the first part of Table 1. The sample is indicated in column (1), the source type is indicated in column (2), the number of sources (or number of measurements for GBH) included in the mean and dispersion is listed in column (3), mean values for the mass accretion rate in dimensionless and physical units are listed in columns (4) and (5), respectively.

For AGN, the dimensionless mass accretion rates are related to AGN type, as is evident from the values listed in the first four lines of Table 1, as expected based on the study by Ho (2009). The 100 FR II sources have the highest mass accretion rates for rates expressed in both dimensionless and physical units. Part of the reason for this is that the sample includes sources with redshifts between about zero and two, as illustrated in Figs 3 and 4, and the

mass accretion rate in physical units increases with redshift. The M03 sample of local AGN has the second highest mass accretion rate, though there is substantial overlap between the M03 and NB16 samples for the mass accretion rate in physical units, and between the M03 sample and both the D19 and NB16 samples for the rate in dimensionless units. The mean dimensionless mass accretion rate for the GBH is similar to that for the AGN and, of course, the rate in physical units is much smaller than that obtained for AGN. The maximum values of the dimensionless mass accretion rate are close to unity, indicating that all of the sources studied here are accreting at Eddington or sub-Eddington levels. This limit is not externally imposed.

It is clear from Figs 3 and 4 that sources with lower values of  $dm/dt$  and  $dM/dt$ , which are evident at low redshift, drop out of each sample as redshift increases. This effect is particularly striking for  $dM/dt$  and is likely a selection effect, whereby sources with lower bolometric disc luminosities or lower radio luminosities that

**Table 5.** Mass accretion rates and efficiency factors for the M03 local sample of AGN.

(1)	(2)	(3)	(4)	(5)	(6)	(7)	(8)	(9)	(10)
Source	Type	$D(\text{Mpc})$	Log ( $\text{dm}/\text{dt}$ )	Log ( $\text{dM}/\text{dt}$ ) ( $M_{\odot} \text{yr}^{-1}$ )	Log ( $\epsilon_{\text{bol}}$ )	Log ( $\epsilon_j$ )	Log ( $\epsilon_j/\epsilon_{\text{bol}}$ )	Log ( $\epsilon_{\text{sd}}$ )	Log ( $M_{\text{dyn}}$ ) ( $M_{\odot}$ )
Ark 564	NS1	106	0.34	-2.27	0.50	-0.87	-1.37	-0.22	6.03
Cyg A	S2/L2	240	-0.84	-0.09	-1.21	-1.00	0.21	0.84	9.40
IC 1459	L2	31	-2.14	-1.79	-3.07	-0.55	2.52	2.58	9.00
IC 4296	L1.9	201	-1.96	-1.51	-2.81	-0.85	1.96	2.10	9.10
IC 4329A	S1	70	0.06	-1.89	0.10	-1.00	-1.10	-0.07	6.69
Mrk 3	S2	56	-1.22	-1.06	-1.76	-1.17	0.59	1.05	8.81
Mrk 279	S1.5	136	-0.32	-1.35	-0.45	-1.66	-1.21	-0.35	7.62
Mrk 335	NS1	115	-0.29	-1.80	-0.42	-1.58	-1.16	-0.29	7.14
Mrk 348	S2	64	-0.49	-1.97	-0.70	-0.38	0.32	1.11	7.17
Mrk 478	NS1	339	-0.12	-1.47	-0.18	-1.57	-1.39	-0.44	7.30
Mrk 507	NS1	231	-0.41	-1.96	-0.59	-1.05	-0.46	0.36	7.10
Mrk 509	NS1	154	-0.30	-1.09	-0.43	-2.27	-1.84	-0.98	7.86
Mrk 590	S1.2	117	-0.21	-1.63	-0.31	-1.44	-1.13	-0.23	7.23
Mrk 766	NS1	55	-0.25	-2.26	-0.36	-1.09	-0.73	0.16	6.64
NGC 315	L1.9	71	-1.76	-1.31	-2.53	-0.52	2.01	2.23	9.10
NGC 1052	L1.9	21	-1.47	-1.83	-2.12	-0.40	1.72	2.07	8.29
NGC 1068	S1.9	15	-1.26	-2.71	-1.81	-0.06	1.75	2.20	7.20
NGC 1275	S2	75	-0.87	-0.87	-1.24	0.01	1.25	1.87	8.64
NGC 1365	S1.8	23	-1.29	-3.07	-1.85	0.07	1.92	2.36	6.87
NGC 1386	S2	12	-1.41	-2.86	-2.02	-1.66	0.36	0.74	7.20
NGC 1667	S2	66	-1.95	-2.67	-2.80	-1.39	1.41	1.56	7.93
NGC 2110	S2	33	-1.10	-1.34	-1.58	-1.52	0.06	0.57	8.41
NGC 2273	S2	30	-1.13	-2.50	-1.61	-1.19	0.42	0.92	7.27
NGC 2787	L1.9	8	-2.49	-3.54	-3.57	-0.60	2.97	2.88	7.59
NGC 2841	L2	13	-2.88	-3.11	-4.15	-1.92	2.23	1.96	8.42
NGC 2992	S2	33	-1.03	-1.93	-1.49	-1.19	0.30	0.85	7.75
NGC 3031	S1.5	4	-1.95	-2.81	-2.81	-1.62	1.19	1.33	7.79
NGC 3079	S2	22	-1.77	-2.77	-2.55	-0.53	2.02	2.24	7.65
NGC 3147	S2	44	-1.66	-1.52	-2.39	-2.05	0.34	0.61	8.79
NGC 3169	L2	18	-1.41	-2.15	-2.02	-2.02	0.00	0.39	7.91
NGC 3226	L1.9	17	-1.79	-2.21	-2.57	-1.95	0.62	0.84	8.23
NGC 3227	S1.5	22	-1.01	-2.07	-1.46	-1.55	-0.09	0.46	7.59
NGC 3516	S1	42	-0.42	-1.71	-0.61	-1.88	-1.27	-0.46	7.36
NGC 3998	L1.9	15	-1.63	-1.52	-2.33	-2.06	0.27	0.55	8.75
NGC 4051	NS1	18	-0.67	-3.05	-0.97	-1.04	-0.07	0.64	6.27
NGC 4117	S2	133	-1.73	-3.64	-2.48	-1.61	0.87	1.12	6.74
NGC 4143	L1.9	18	-2.12	-2.45	-3.04	-1.74	1.30	1.37	8.32
NGC 4151	S1.5	22	-0.69	-1.69	-1.00	-1.53	-0.53	0.16	7.65
NGC 4203	L1.9	15	-1.86	-2.61	-2.68	-1.85	0.83	1.02	7.90
NGC 4258	S1.9	8	-1.62	-2.67	-2.33	-2.40	-0.07	0.22	7.60
NGC 4261	L2	32	-1.81	-1.74	-2.61	-0.96	1.65	1.85	8.72
NGC 4278	L1.9	10	-2.51	-1.95	-3.60	-1.69	1.91	1.81	9.20
NGC 4374	L2	20	-2.35	-1.80	-3.38	-1.19	2.19	2.15	9.20
NGC 4388	S2	18	-0.37	-2.22	-0.54	-2.12	-1.58	-0.75	6.80
NGC 4450	L1.9	18	-1.57	-2.92	-2.26	-1.73	0.53	0.84	7.30
NGC 4486	L2	17	-2.38	-1.55	-3.42	-0.74	2.68	2.64	9.48
NGC 4501	S2	18	-1.84	-2.59	-2.65	-2.29	0.36	0.55	7.90
NGC 4548	L2	18	-1.84	-3.09	-2.64	-1.72	0.92	1.11	7.40
NGC 4565	S1.9	10	-2.06	-3.00	-2.95	-1.91	1.04	1.14	7.70
NGC 4579	S1.9	18	-1.47	-2.27	-2.11	-1.56	0.55	0.90	7.85
NGC 4594	L2	11	-2.14	-1.75	-3.07	-1.95	1.12	1.19	9.04
NGC 4736	L2	5	-1.87	-3.22	-2.68	-2.68	0.00	0.18	7.30
NGC 5033	S1.5	20	-1.30	-2.65	-1.87	-1.81	0.06	0.49	7.30
NGC 5194	S2	8	-1.63	-3.38	-2.34	-2.01	0.33	0.61	6.90
NGC 5252	S2	99	-0.83	-1.36	-1.19	-1.52	-0.33	0.30	8.12
NGC 5347	S2	33	-1.47	-3.41	-2.10	-0.81	1.29	1.65	6.70
NGC 5548	S1.5	75	-0.56	-1.17	-0.79	-1.98	-1.19	-0.43	8.03
NGC 5929	S2	36	-1.39	-2.82	-2.00	-0.54	1.46	1.85	7.22
NGC 6166	S2	124	-2.26	-1.71	-3.24	-0.45	2.79	2.80	9.19
NGC 6251	S2	102	-1.42	-1.33	-2.03	-0.12	1.91	2.29	8.73

Table 5 – continued

(1)	(2)	(3)	(4)	(5)	(6)	(7)	(8)	(9)	(10)
Source	Type	$D(\text{Mpc})$	Log $(dm/dt)$	Log $(dM/dt)$ $(M_{\odot} \text{ yr}^{-1})$	Log $(\epsilon_{\text{bol}})$	Log $(\epsilon_j)$	Log $(\epsilon_j/\epsilon_{\text{bol}})$	Log $(\epsilon_{s/d})$	Log $(M_{\text{dyn}})$ $(M_{\odot})$
NGC 6500	L2	43	-2.07	-2.44	-2.97	-0.49	2.48	2.57	8.28
NGC 7469	S1	71	-0.15	-1.99	-0.22	-1.31	-1.09	-0.16	6.81
NGC 7672	S2	57	-0.12	-1.97	-0.18	-2.15	-1.97	-1.03	6.80
NGC 7743	S2	26	-1.49	-3.67	-2.14	-0.64	1.50	1.84	6.47
PG 0026+129	Q	672	-0.07	-0.99	-0.09	-1.02	-0.93	0.04	7.73
PG 0052+251	Q	739	-0.23	-0.54	-0.32	-2.01	-1.69	-0.79	8.34
PG 0804+761	Q	461	-0.37	-0.73	-0.52	-1.82	-1.30	-0.46	8.28
PG 0844+349	Q	287	-0.38	-1.69	-0.54	-1.80	-1.26	-0.43	7.34
PG 0953+414	Q	1198	-0.26	-0.65	-0.37	-1.38	-1.01	-0.12	8.26
PG 1211+143	Q	388	-0.36	-1.40	-0.51	0.05	0.56	1.40	7.61
PG 1226+023	Q	755	0.04	0.13	0.05	0.66	0.61	1.62	8.74
PG 1229+204	Q	287	-0.19	-0.96	-0.27	-2.29	-2.02	-1.11	7.88
PG 1307+085	Q	739	-0.33	-0.54	-0.47	-2.33	-1.86	-1.00	8.44
PG 1411+442	Q	407	-0.51	-1.26	-0.73	-1.81	-1.08	-0.30	7.90
PG 1426+015	Q	392	-0.68	-0.66	-0.97	-2.21	-1.24	-0.54	8.67
PG 1613+658	Q	605	-0.37	-0.64	-0.54	-1.67	-1.13	-0.30	8.38
PG 2130+099	Q	273	-0.61	-1.10	-0.87	-1.84	-0.97	-0.23	8.16
3C 120	S1	148	-0.27	-1.18	-0.38	0.18	0.56	1.44	7.73
3C 390.3	S1	258	-0.58	-0.69	-0.82	-0.64	0.18	0.93	8.53
Sgr A*		0.008	-4.18	-6.23	-6.01	-1.34	4.67	3.84	6.60

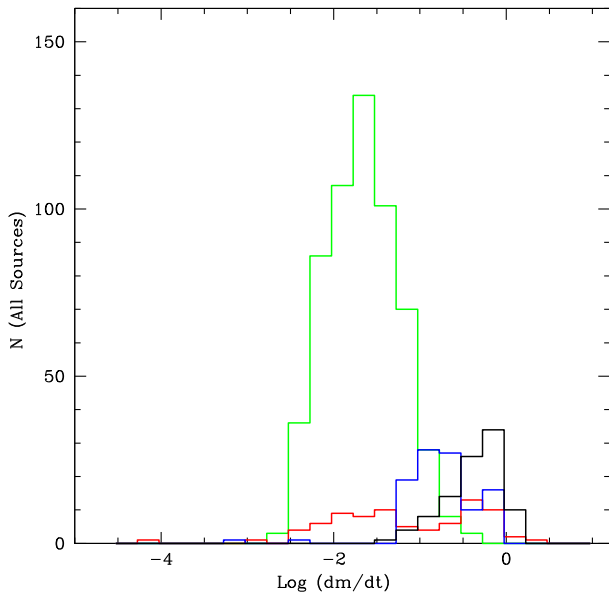


**Figure 1.** Histograms of the dimensionless mass accretion rate,  $\dot{m} \equiv dm/dt$ . Here and throughout the paper, the NB16 sample of 576 LINERs is shown in green; the D16/D19 sample of 100 FR II sources is shown in black; the M03 local sample of 80 AGN is shown in red; and the S15 sample of 103 measurements of 4 GBH is shown in blue.

are at larger distances and redshift require observations to lower flux densities to be detected, and thus in flux limited surveys these sources drop out of the sample as redshift increases. Thus, the different distributions of  $dM/dt$  seen in Fig. 4 is affected by these redshift selection effects. However, the upper envelope of the distributions seen in Fig. 4 indicates the maximum mass accretion rates for each of the source types as a function of redshift.

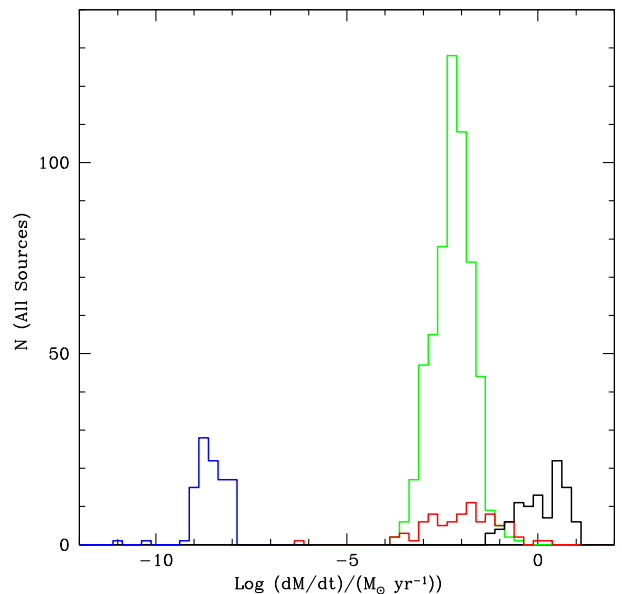


**Figure 2.** Histograms of the mass accretion rate,  $dM/dt$ , in physical units of solar masses per year; sample colours are as in Fig. 1.

Some of the sources studied here have mass accretion rates obtained using independent methods, such as those discussed by Jiang et al. (2019) and Raimundo et al. (2012). These studies are based on a detailed accretion disc model of each source. The model includes numerous accretion disc parameters in addition to the mass accretion rate. In addition, the bolometric accretion disc luminosity is based on the optical properties of the accretion disc, and a detailed model of the disc, as described below. Thus, the method and its application are quite different from those applied here, which are summarized in Sections 1.1, 2, 3.1, and 3.2. There are 14

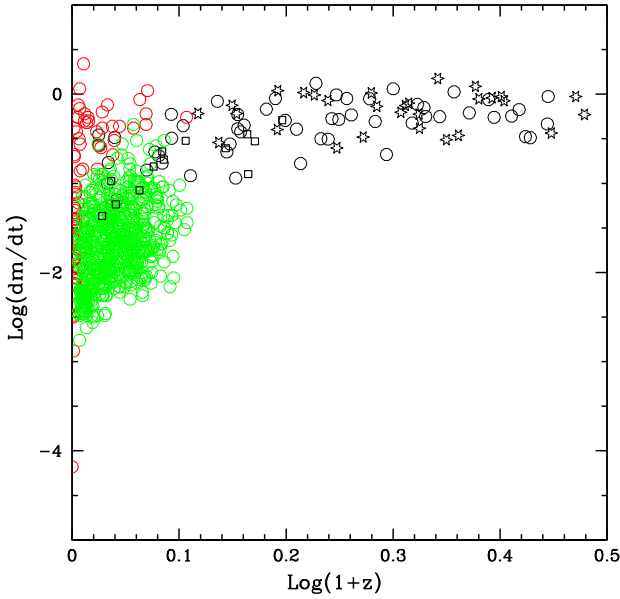


**Figure 3.** The dimensionless mass accretion rate,  $dm/dt$ , is shown as a function of  $(1+z)$  for the AGN samples. Classical double (FRII) LEG, HEG, and quasar (Q) source types are shown in black as open squares, open circles, and open stars, respectively. **M03** and **NB16** sources are shown as red and green open circles, respectively.

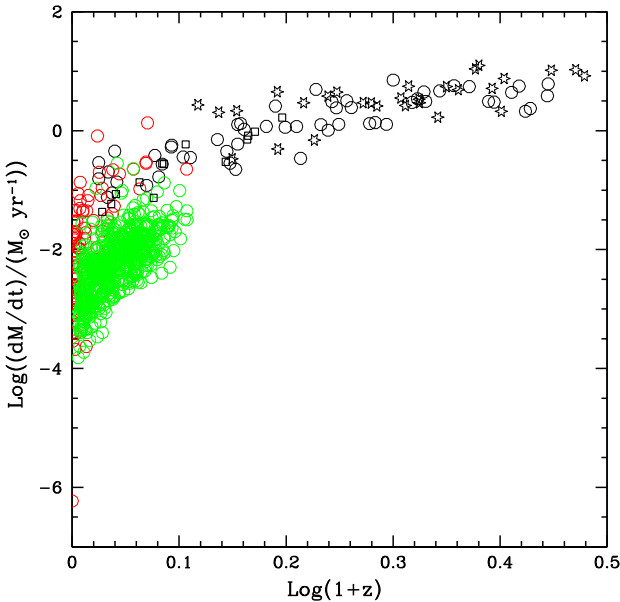


**Figure 4.** The mass accretion rate,  $dM/dt$ , in physical units of solar masses per year is shown as a function of  $(1+z)$  for the AGN samples; colours and symbols are as in Fig. 3.

independently determined values of mass accretion rates that overlap with 13 sources studied here (one source is included twice), and these are listed in Table 2. In Table 2, J19 refers to Jiang et al. (2019); (T5) refers to Table 5 (presented here and included below); R12(T1), R12(T2), and R12(T3) refer to tables 1, 2 and 3 of Raimundo et al. (2012), respectively; the comparison of efficiency factors is discussed in Section 4.2. The methods used by Jiang et al. (2019) and Raimundo et al. (2012) are based on optical observations and have completely different functional forms compared with those applied here (see

equation 3 of Raimundo et al. 2012; see also Davis & Laor 2011; and Netzer & Trakhtenbrot 2014), so their mass accretion rate and efficiency factor determinations are independent of those obtained here.

Values of the mass accretion rate obtained with independent methods are similar, within factors of few, for 12 of the 14 comparisons (see Table 2); two sources differ by about a factor of 10. Given the very different way that the accretion rates are obtained, this agreement suggests that both methods provide reliable estimates of mass accretion rates. Note that time variability may be a factor, as observations used to determine the accretion rate of a given source with different methods were obtained at different times. Thus, it is likely that each method provides mass accretion rate estimates that are accurate to factors of about a few.

The second part of Table 1 lists mean values and dispersions obtained with multiple simultaneous radio and X-ray measurements of each GBH. For the stellar-mass GBH, the dimensionless mass accretion rates are about 0.2 for GX-339-4; 0.1 for V404 Cyg; 0.08 for J1118+480; and 0.01 for A0 6200. These values are consistent with expectations for black hole X-ray binaries in the low hard state (e.g. Skipper & McHardy 2016), and are similar to the accretion and mass transfer rates from the companion star to the black hole discussed by McClintock et al. (2003) and Shao & Li (2020). The mean accretion rate in physical units for 103 measurements of four stellar-mass GBH is about  $3 \times 10^{-9} M_{\odot} \text{ yr}^{-1}$ , with three of the four stellar-mass GBH having quite similar values, and one source, A0 6200, having a lower mean value that results from two very different accretion rates of about  $5 \times 10^{-9} M_{\odot} \text{ yr}^{-1}$  and  $10^{-11} M_{\odot} \text{ yr}^{-1}$  (see Table 3). The input values for the GBH were adopted from S15, who considered GBH with simultaneous radio and X-ray data that were in the low-hard state (see S15 for details), thus the mass accretion rates obtained here apply to rates during that phase. The typical values obtained here based on 76 simultaneous radio and X-ray measurements of the source for GX 339-4 fall into a range that is intermediate between previously reported values (e.g. Zdziarski, Ziolkowski, & Mikolajewska 2019), which are obtained with methods independent of those introduced by D16 and D19, and applied here. Similarly, values obtained here for A0 6200 and V404 Cyg are within the range of values for these sources discussed by Lasota (2000) and Ziolkowski & Zdziarski (2018). In all cases, the values obtained here only depend upon the identification of the term  $(B/B_{\text{edd}})^2$  from equation (1) with the empirically determined quantity  $(L_{\text{bol}}/L_{\text{Edd}})^A$  (see equation 2) as discussed in detail by D19, and thus are independent of a detailed accretion disc or mass transfer model for the systems, so the agreement is encouraging.

Mass accretion rates for sub-types of AGN for the FRII sources and the **M03** sources are included in the third and fourth sections of Table 1; the sources from the **NB16** sample are all one type of AGN, LINERS, so results from sub-types of the FRII and **M03** samples can be compared with those for the LINERS. For the FRII sources, the quasars (Q) and W galaxies, which have weak emission lines as defined by Grimes et al. (2004), have the highest dimensionless mass accretion rates, though within the one sigma standard deviation for the sub-sample the rates are similar for the different types of sources. Of the FRII sources, for accretion rates in physical units of  $M_{\odot} \text{ yr}^{-1}$ , quasars have the highest accretion rates, followed by high excitation galaxies (HEG), W, and low excitation galaxies (LEG) sources (e.g. Mingo et al. 2014; Fernandes et al. 2015).

For the **M03** sample, the quasars and NS1 sources have the highest dimensionless mass accretion rates, followed by S(1–1.9) and S2 sources, and L1.9–L2 sources (with the source types defined by **M03**). Mean values and the dispersions of accretion rates in both

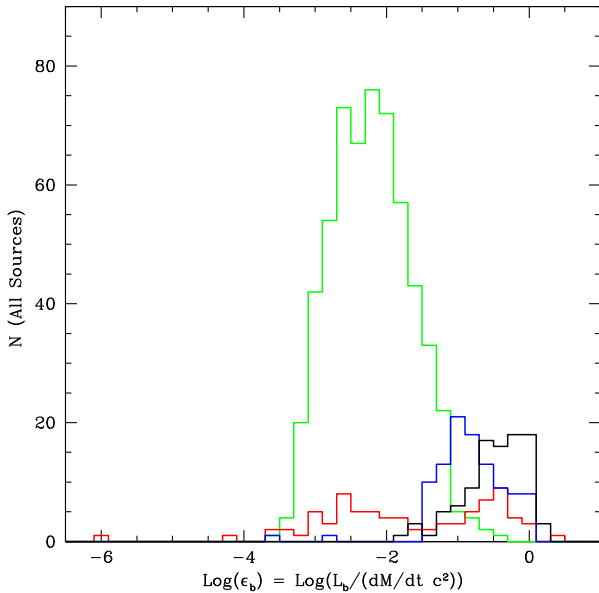


**Figure 5.** Histograms of the bolometric efficiency factor,  $\epsilon_{\text{bol}}$ , defined by equation (9) (see also equation 5); sample colours are as in Fig. 1.

dimensionless and physical units for the **M03** L type sources are similar to that obtained for the 576 LINERs in the **NB16** sample. Mass accretion rates in physical units of all of the **M03** source types are similar to each other and to that of the **NB16** LINER sample, with the exception of the **M03** quasars, which have rates about an order of magnitude larger than the other **M03** source types studied here.

#### 4.2 Efficiency factors

Histograms illustrating the efficiency factors are shown in Figs 5–8. The mean value and dispersion for the efficiency factors  $\epsilon_{\text{bol}}$ ,  $\epsilon_j$ , the ratio  $\epsilon_j/\epsilon_{\text{bol}}$ , and  $\epsilon_{\text{sl/d}}$ , defined in Section 3.2, are listed in columns (6)–(9) of Table 1 for the samples and sources discussed in Section 4.1, as described above.

The efficiency factor for the bolometric luminosity of the accretion disc, shown in Fig. 5 and listed in column (6) of Table 1 indicates a significant overlap of values for the FRII sources and GBH. The **M03** local sample of AGN appears to split into two components, with a break at  $\epsilon_{\text{bol}} \approx -1.5$ . The higher efficiency factor component is similar to that of the FRII sources, while the lower efficiency factor component is similar to that of the **NB16** LINER sample. To study this further, values of  $\epsilon_{\text{bol}}$  for each of the GBH, and different categories of AGN for the FRII and **M03** samples are listed in Table 1. The Q, NS1, and S(1–1.9) from the **M03** sample overlap with the FRII sources, while the L1.9, L2, and S2 **M03** sources overlap with the **NB16**. A similar trend is seen for the dimensionless mass accretion rates. This is not the case for the mass accretion rates in physical units, where the **NB16** LINERs and **M03** sample show significant overlap, while the FRII sources and GBH have little overlap with other types of sources. The fact that the mean values of  $\epsilon_{\text{bol}}$  for the samples are quite different, and that the dispersion of each of the samples and subsamples is large, indicates that a constant value of  $\epsilon_{\text{bol}}$  does not provide an accurate description of these sources. Splitting the samples into sub-sets, as shown in Table 1 for the GBH, FRII, and **M03** sources may provide a way to estimate  $\epsilon_{\text{bol}}$  for each sub-type. Of course, the entire sample of LINERs is one sub-type of AGN.

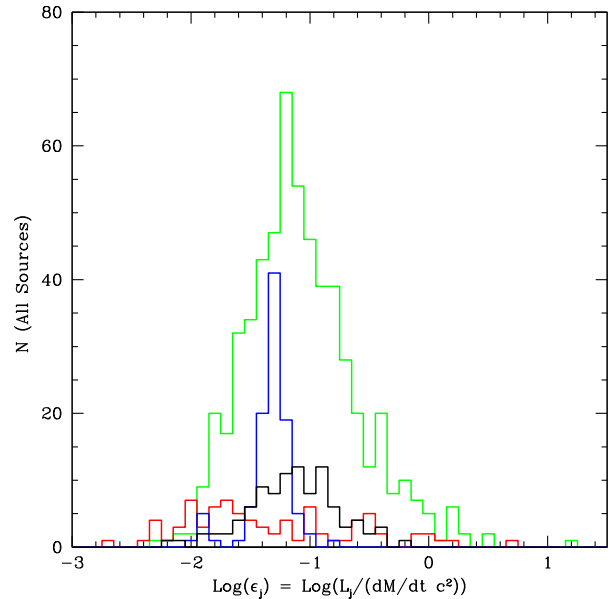


**Figure 6.** Histograms of the outflow efficiency factor,  $\epsilon_j$ , defined in the traditional manner (see equation 10); sample colors are as in Fig. 1.

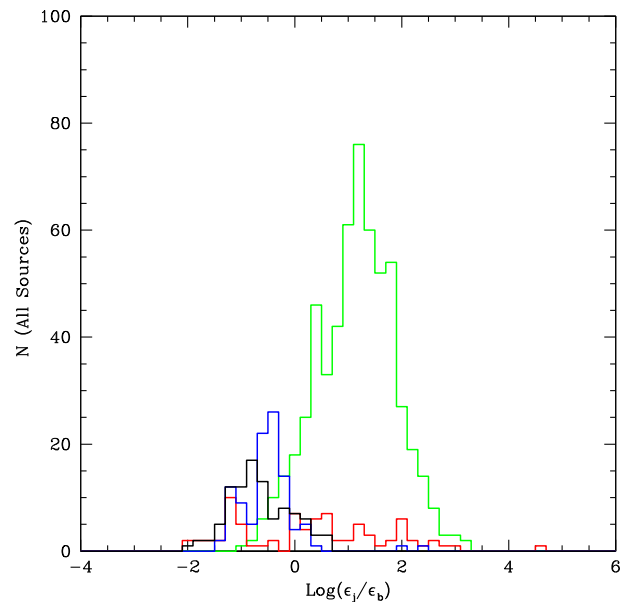


**Figure 7.** Histograms of the ratio of the outflow to the bolometric efficiency factor,  $\epsilon_j/\epsilon_{\text{bol}}$ , or  $L_j/L_{\text{bol}}$ ; sample colours are as in Fig. 1.

The efficiency factor of radiation from the accretion disc,  $\epsilon_{\text{bol}}$ , for some sources studied here were obtained by Raimundo et al. (2012) using methods that are independent of those developed and applied here. Raimundo et al. (2012) used two different methods to obtain bolometric disc luminosities, and the resulting efficiency factors are listed in Tables 2 and 3 of that paper, referred to here as R12(T2) and R12(T3). A comparison of efficiency factors for three sources that are in both R12(T2) and R12(T3) indicate that their efficiency factors internally agree to a factor of about 1.5–2. Accretion disc efficiency factors for sources studied here that overlap with those studied by Raimundo et al. (2012) are included in columns (6)–(10) of the second part of Table 2; there (T5) refers to Table 5 (presented here and included below). The ratio of values obtained here to those

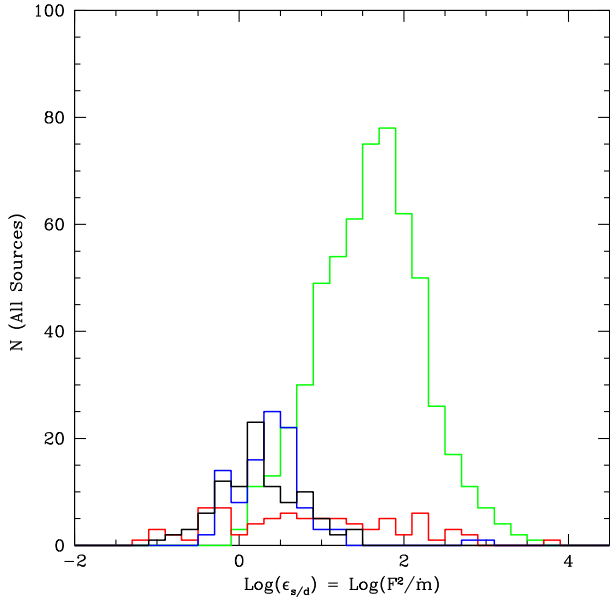


**Figure 8.** Histograms of the ‘spin relative to disc’ efficiency factor,  $\epsilon_{sl,d}$ , defined by equation (11) that measures the relative contribution of spin and dimensionless mass accretion rate to the Eddington normalized beam power,  $L_j/L_{\text{Edd}}$ ; sample colours are as in Fig. 1. This efficiency factor may be written as  $g_j^{-1} (L_j/L_{\text{bol}})(L_{\text{bol}}/L_{\text{Edd}})^{1-2A}$  and thus is similar to  $10 \epsilon_j/\epsilon_{\text{bol}}$  since  $g_j$  is taken to be 0.1 as in D19.

listed in R12(T2) and R12(T3) are listed in columns (8) and (10) of Table 2, respectively. Most of the sources agree to a factor of a few, which is reasonably good agreement considering that it is similar to the internal consistency of the comparison sample, and considering that the observations used in the different studies were obtained at different times, and the sources may be intrinsically time variable.

The beam power efficiency factors are shown in Fig. 6 and are listed in column (7) of Table 1. These are proportional to  $F^2$  (see equation 10). Remarkably, the mean values of  $\epsilon_j$  for all of the samples and source types are consistent given the dispersion of each sample. Each AGN sample has a rather broad range of values, which is reflected in the large dispersion of each sample. Thus, though the mean values of  $\epsilon_j$  are similar for all source samples and types studied, the large dispersion of the AGN samples and sub-types would have to be taken into account before assuming and applying a value for similar sources. The dispersion of the GBH is relatively small, and the values presented here for the GBH could provide a reliable estimate of  $\epsilon_j$  (i.e.  $F^2$ ) for similar sources.

The ratio  $\epsilon_j/\epsilon_{\text{bol}}$  (i.e.  $L_j/L_{\text{bol}}$ ) is shown in Fig. 7 and values are listed in column (8) of Table 1. The values for the GBH and FR II sources have substantial overlap, and one component of the M03 sources also overlaps with these sources. A long tail of values for the M03 sample overlaps with the NB16 LINERs. This quantity essentially separates sources into disc dominated sources and jet dominated sources. Sources with  $\epsilon_j/\epsilon_{\text{bol}} > 1$  are jet dominated, and those with  $\epsilon_j/\epsilon_{\text{bol}} < 1$  are disc dominated (see also D18). Clearly, most of the LINERs and some of the M03 sources are jet dominated, most by a very large factor of 10 to 100. Outflow from these sources are almost certainly powered by black hole spin, as discussed in Section 1.1 (see also Section 1.1 of D19). Other sources with very large values of this quantity include A0 6200, and the M03 L1.9, L2, and S2 sources. Sources with values less than one include FR II sources of all types, most of the GBH, and the M03 Q, and NS1 sources, while

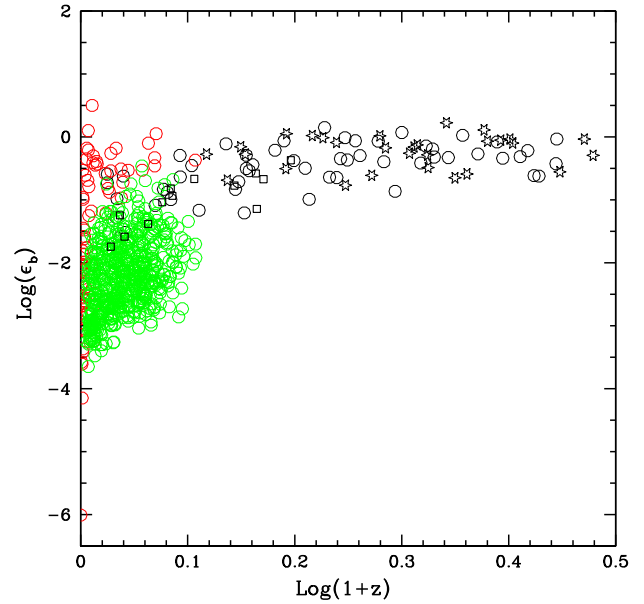


**Figure 9.** The bolometric efficiency factor,  $\epsilon_{\text{bol}}$ , is shown as a function of  $(1+z)$  for the AGN samples; colours and symbols are as in Fig. 3.

the S(1-1.9) sources have a mean value near 1 and a very large dispersion.

Another measure of interest is the relative input to the Eddington-normalized outflow beam power from black hole spin and from the accretion disc. Equation (1) may be written as  $(L_j/L_{\text{Edd}}) = g_j(dm/dt)F^2$ , so one measure of this relative input is given by  $\epsilon_{sl,d}$ , defined by equation (11). Values of this quantity are listed in column (9) of Table 1. Almost all of the sources have values of  $\epsilon_{sl,d}$  that are greater than 1. Types that include values less than one include about half of the FR II quasars (Q), the 3 FR II W sources, and some of the M03 Q and NS1 sources. This highlights the role of black hole spin as the source that powers the outflow and the role of the accretion disc as the source that maintains the magnetic field that is anchored in the disc and threads the black hole. Note that in the model described by Meier (1999), both a disc wind, as in the model of Blandford & Payne (1982), and spin energy extraction from the black hole, as in the model of Blandford & Znajek 1977, power the outflow, and this model is also described by equation (1), as discussed in detail by D19 Section 4 (see also Meier 1999).

## 5 DISCUSSION

In addition to considering histograms of quantities, it is helpful view the redshift distributions of the sources to get a sense of contributions to the histograms from sources at different redshift. The GBH are located in the Galaxy, so these are not including in the redshift distributions shown in Figs 3, 4, and 9–13. The M03 sources are quite local, and include sources with a wide range of intrinsic parameters. The NB16 sources extend to a redshift of about 0.3, with this cut-off imposed by NB16 for this study. The D19 sources extend to a redshift of about 2. For some parameters, it is easy to see the impact of missing lower luminosity sources as redshift increases, while other parameters do not have a strong redshift dependence. For sources that increase with redshift, the upper envelope of the distributions provides a guide as to how parameters that describe the most luminous and radio bright sources evolve with redshift.

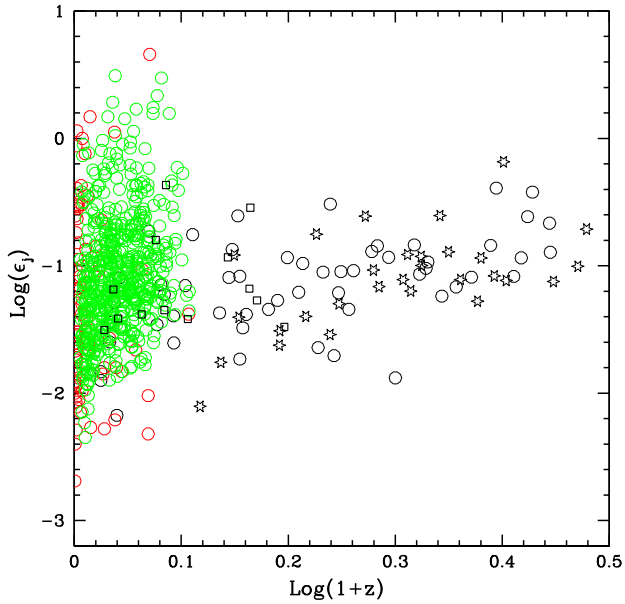


**Figure 10.** The outflow efficiency factor,  $\epsilon_j$ , is shown as a function of  $(1+z)$  for the AGN samples; colors and symbols are as in Fig. 3.

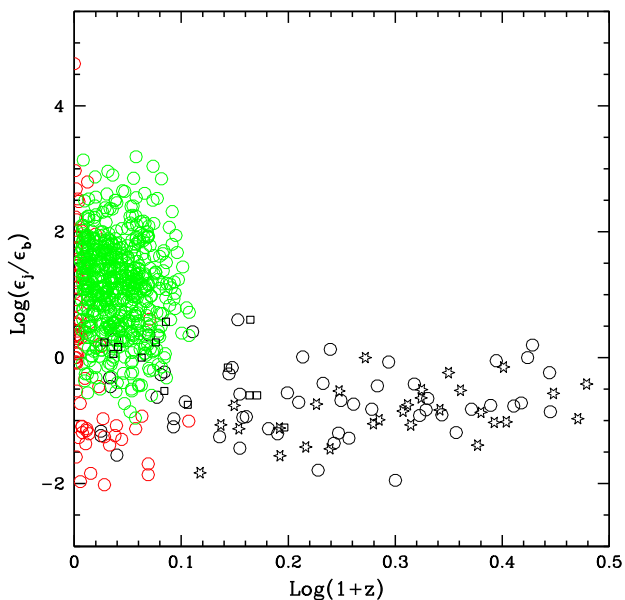


**Figure 11.** The ratio of the outflow to the bolometric efficiency factor,  $\epsilon_j/\epsilon_{bol} = L_j/L_{bol}$ , is shown as a function of  $(1+z)$  for the AGN samples; colors and symbols are as in Fig. 3.

It is clear from Fig. 4 that sources at higher redshift have higher mass accretion rates physical units, so the high-mass accretion rates seen in Fig. 2 are due to these sources. The low-redshift sample of M03 suggests that there are sources at all accretion rates and that the lower luminosity sources that are associated with lower mass accretion rates are missing at higher redshift due to the flux limited nature of the samples that include higher redshift sources. Fig. 3 shows the dimensionless mass accretion rate as a function of redshift. Clearly, there is a rather sharp boundary at  $dm/dt = 1$ , and this is not artificially imposed, but is an empirical result and reflects that very sharp boundary found by D16, D18, and D19 when the bolometric

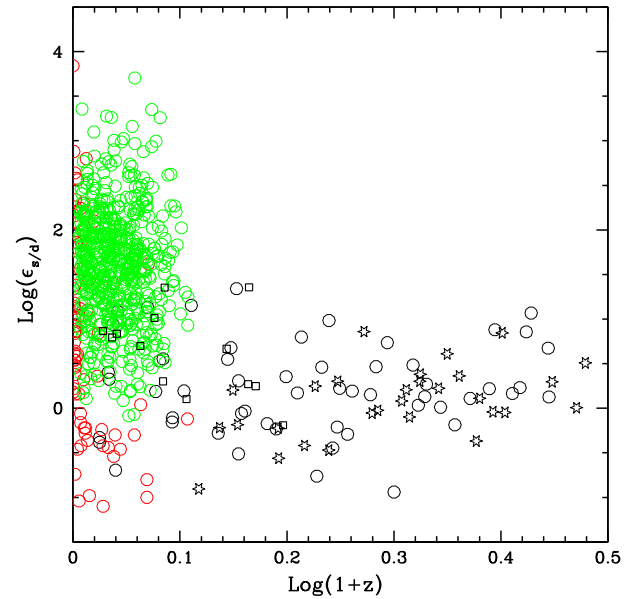


**Figure 12.** The spin relative to disc efficiency factor,  $\epsilon_{s/d}$ , which can be rewritten as  $\epsilon_{s/d} = g_j^{-1} (L_j/L_{bol}) (L_{bol}/L_{Edd})^{1-2A}$  with  $g_j = 0.1$ , is similar to  $\epsilon_j/\epsilon_{bol}$  and is shown as a function of  $(1+z)$  for the AGN samples; colours and symbols are as in Fig. 3.

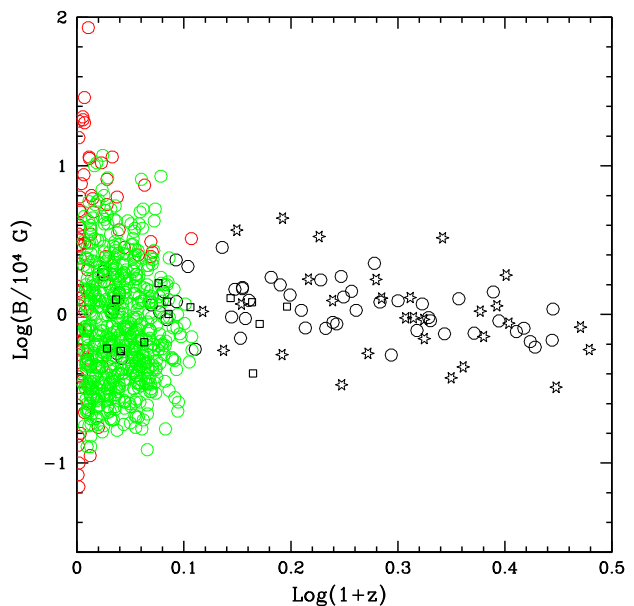


**Figure 13.** The accretion disc magnetic field strength at the location where the field that taps the black hole spin is anchored in the disc in units of  $10^4$  G as a function of  $(1+z)$  for the AGN samples; colours and symbols are as in Fig. 3.

disc luminosity approaches the Eddington luminosity. While  $dM/dt \propto M_{dyn}(dm/dt)$ , the accretion disc magnetic field strength  $B$  in physical units is obtained from  $B^2 \propto M_{dyn}^{-1}(dm/dt)$ , which accounts for the redshift distribution of FRII sources seen in Fig. 13. This suggests a weak dependence of the disc magnetic field strength,  $B$ , in physical units on redshift.

The efficiency factors are shown as a function of redshift in Figs 9–12. Fig. 9 reflects the fact that there are no super-Eddington sources. There is a narrow range of values for the FRII sources with little

or no redshift evolution. It is clear that **NB16** LINERs with lower values of  $\epsilon_{\text{bol}}$  that are present near zero redshift have dropped out by a redshift of about 0.3, most likely reflecting a selection effect whereby lower luminosity sources are not included in the sample as redshift increases (**NB16**). Redshift selection effects for  $\epsilon_j$  and  $\epsilon_j/\epsilon_{\text{bol}}$  for each sample separately are much less pronounced, especially that for  $\epsilon_j/\epsilon_{\text{bol}}$ , compared with that for  $\epsilon_{\text{bol}}$ .

## 6 SUMMARY AND CONCLUSIONS

The outflow method allows empirical estimates of the accretion disc magnetic field strength in Eddington units,  $(B/B_{\text{Edd}})$ , at the location where the magnetic field that torques the black hole is anchored in the disc (**D19**). Interestingly, two key physical parameters describing the accretion disc can be obtained from this ratio: the magnetic field strength in physical units and the mass accretion rate in physical units. As shown in Sections 1.1 and 3.1, the mass accretion rate in physical units is  $dM/dt \propto L_{\text{Edd}}(B/B_{\text{Edd}})^2$ , whereas the accretion disc magnetic field strength in physical units is  $B^2 \propto L_{\text{Edd}}^{-1}(B/B_{\text{Edd}})^2$  (**D19**). So, three important physical quantities that describe the accretion disc follow from empirical estimates of  $(B/B_{\text{Edd}})^2$ : the dimensionless mass accretion rate; the mass accretion rate in physical units; and the disc magnetic field strength in physical units (disc magnetic pressure in physical units). Here, data for three samples of AGN, including 756 supermassive black hole systems, and 103 measurements of 4 stellar mass black holes, referred to as GBH, are used to obtain and study mass accretion rates and efficiency factors, while the magnetic field strength in physical and dimensionless units are discussed by **D19**.

Mass accretion rates in dimensionless units can be divided into five categories, defined here as high ( $\text{Log}(\dot{m}) \geq -0.5$ ), medium-high ( $-0.5 > \text{Log}(\dot{m}) \geq -1.0$ ), medium ( $-1.0 > \text{Log}(\dot{m}) \geq -1.5$ ), medium-low ( $-1.5 > \text{Log}(\dot{m}) \geq -2.0$ ), and low ( $\text{Log}(\dot{m}) < -2.0$ ). Broadly, sources fall into the following categories: all FRII sources (except LEG), and **M03** NS1 and Q sources have high  $\text{Log}(\dot{m})$ ; three GBH (all except A06200), the **D16/19** FRII LEG, and the **M03** S(1–1.9) sources have medium-high  $\text{Log}(\dot{m})$ ; the **M03** S2 sources have medium  $\text{Log}(\dot{m})$ ; GBH A0 6200, the **NB16** LINERs, and **M03** L1.9 and L2 sources have medium-low  $\text{Log}(\dot{m})$ ; a few individual sources have low  $\text{Log}(\dot{m})$  (see Tables 3–5 and 6 (online in supplementary material)).

Mass accretion rates in physical units for the AGN studied here seem to have distinct mean values, but with a broad dispersion, as is evident in Fig. 2, and appear to fall into four broad categories: high, medium, low, and very low. Sources with high-mass accretion rates, where  $dM/dt$  is in units of  $M_{\odot} \text{ yr}^{-1}$ , have ( $\text{Log}(dM/dt) > 0$ ) and include FRII Q and some HEG; sources with medium rates of about ( $0 > \text{Log}(dM/dt) > -1$ ) include FRII LEG, W, and some HEG types and **M03** Q types; sources with mean values in the low range from ( $-1 > \text{Log}(dM/dt) > -2$ ) are practically absent; and sources with very low rates of about ( $\text{Log}(dM/dt) < -2$ ) include the **NB16** LINERs and all of the **M03** sources except Q type. Though sources with mean values in the low range are practically absent, many individual sources fall into this range and are evident in the dispersion of the mean values of  $dM/dt$ . The GBH all have very similar mass accretion rates of about  $\text{Log}(dM/dt) \approx -8.5$ , with a few individual observations stretching to very low values of about ( $10^{-10}$ – $10^{-11}$ ), for example one observation of A0 6200 and one of V404 Cyg (see Table 3).

Efficiency factors associated with the bolometric luminosity of the accretion disc have a broad range, and may be categorized as high ( $\text{Log}(\epsilon_{\text{bol}}) > -1$ ), medium ( $-1 > \text{Log}(\epsilon_{\text{bol}}) > -2$ ), and low

( $\text{Log}(\epsilon_{\text{bol}}) < -2$ ). Sources with high values include most or all of the FRII sources (except about half of the FRII LEG, which fall into the medium category), GX 339–4, about half of the observations of V404 Cyg, and the **M03** NS1 and Q sources. Sources in the medium category include about half of the FRII LEG sources and about half of the V404 Cyg observations, J1118+480, and the **M03** S(1–1.9) and S2 types. Sources in the low category include the **NB16** LINERs, A0 6200, and the **M03** L1.9 and L2 types.

The mean values of efficiency factors associated with collimated outflows,  $\epsilon_j$ , defined in the traditional manner in terms of mass accretion rate, have a small range of mean values and a large dispersion per sample (see the first four lines of Table 1 and Fig. 6). This efficiency factor measures the beam power relative to the mass accretion rate in physical units. In the spin powered outflow model described in Section 1.1, the accretion disc plays the role of maintaining the magnetic field; the field is anchored in the disc and threads the black hole, exerting a torque and producing the outflow (Blandford & Znajek 1977), while it is the spin energy of the hole that powers the outflow. In the Meier model (1999), the outflow is powered by both the spin of the black hole and a disc wind, with the disc wind component similar to that of Blandford & Payne model (1982). The Meier model has the same functional form as the Blandford & Znajek model, but has a different constant of proportionality, and thus is described by equation (1); the different expected constants of proportionality as compared with the empirically determined constant of proportionality is discussed in detail by **D19**.

A measure of the outflow power sourced to the black hole spin relative to that contributed by the disc is the efficiency factor  $\epsilon_{s/d}$ , listed in column (9) of Table 1. All of the samples, and most of the sub-samples, have mean values of  $\text{Log}(\epsilon_{s/d}) > 0$ , indicating that most of the outflow beam power originates from the black hole spin. The exceptions are the 3 FRII W sources, and a subset of the 20 **M03** NS1 and Q sources.

The ratio  $\epsilon_j/\epsilon_{\text{bol}} = L_j/L_{\text{bol}}$  was studied in detail by **D18**. As discussed in that work, sources with  $\epsilon_j/\epsilon_{\text{bol}} > 1$  are jet dominated sources, while those with  $\epsilon_j/\epsilon_{\text{bol}} < 1$  are disc-dominated sources. The results obtained by **D18** align quite well with previously published results, such as those discussed by Heckman & Best (2014) and **NB16**. The results obtained here indicate that both disc-dominated and jet-dominated sources have outflow beam powers with a spin term that exceeds the disc term, indicated by a value of ( $\epsilon_{s/d} > 1$ ). That is, almost all of the sources with  $\epsilon_j/\epsilon_{\text{bol}} > 1$  have ( $\epsilon_{s/d} > 1$ ), and many sources with  $\epsilon_j/\epsilon_{\text{bol}} < 1$  have ( $\epsilon_{s/d} > 1$ ) including three of the GBH, all of the FRII sources except the W types, and almost all of the **M03** types except some of the NS1 and Q **M03** sources.

Parameters with a dispersion that is not too large could provide estimates of this parameter for additional sources of the same type. If the parameter evolves with redshift, then this should only be applied to sources of the same type within a similar redshift range. To identify such source types, consider quantities with a dispersion less than about 0.5 dex to one significant figure. This suggests that the quantities that could be applied to other sources of the same type are for **NB16** LINERs,  $\text{Log}(\dot{m})$ ,  $\text{Log}(dM/dt)$ , and  $\epsilon_j$ ; for FRII sources,  $\text{Log}(\dot{m})$ ,  $\epsilon_{\text{bol}}$ ,  $\epsilon_j$ , and  $\epsilon_{s/d}$ ; for **M03** sources, none for the full sample but may be applied to sub-samples; for the GBH,  $\text{Log}(\dot{m})$ ,  $\text{Log}(dM/dt)$ ,  $\epsilon_{\text{bol}}$ ,  $\epsilon_j$ , and  $\epsilon_{s/d}$ . The results obtained here suggest that black hole systems with powerful outflows provide an interesting and important guide for mass accretion rates and efficiency factors that may be applied to additional sources for some source types.

## ACKNOWLEDGEMENTS

Thanks are extended to the referee for very helpful comments and suggestions. It is a pleasure to thank the many colleagues with whom this work was discussed, especially Jean Brodie, George Djorgovski, Megan Donahue, Yan-Fei Jiang, Syd Meshkov, Chiara Mingarelli, Chris O’Dea, Masha Okounkova, David Spergel, Alan Weinstein, and Rosie Wyse. I would especially like to thank Jerry Ostriker for helpful discussions related to the topics discussed in this paper. The Flatiron Institute is supported by the Simons Foundation. This work was also supported in part by the Losoncy Fund and the PSU Berks Advisory Board, and was performed in part at the Aspen Center for Physics, which is supported by National Science Foundation grant no. PHY-1607611.

## DATA AVAILABILITY STATEMENT

The data underlying this article are available in the article or are listed in [D19](#).

## REFERENCES

- Begelman M. C., Blandford R. D., Rees M. J., 1984, *RvMp*, 56, 255  
 Bian W.-H., Zhao Y.-H., 2003, *PASJ*, 55, 599  
 Blandford R. D., 1990, in Courvoisier T. J. L., Mayor M., eds, *Active Galactic Nuclei*. Springer, Berlin, p. 161  
 Blandford R. D., Payne D. G., 1982, *MNRAS*, 199, 883  
 Blandford R. D., Znajek R. L., 1977, *MNRAS*, 179, 433  
 Corbel S., Körding E., Kaaret P., 2008, *MNRAS*, 389, 1697  
 Corbel S., Coriat M., Brocksopp C., Tzioumis A. K., Fender R. P., Tomsick J. A., Buxton M. M., Bailyn C. D., 2013, *MNRAS*, 428, 2500  
 Daly R. A., 2009, *ApJ*, 696, L32  
 Daly R. A., 2011, *MNRAS*, 414, 1253  
 Daly R. A., 2016, *MNRAS*, 458, L24  
 Daly R. A., 2019, *ApJ*, 886, 37  
 Daly R. A., Sprinkle T. B., 2014, *MNRAS*, 438, 3233  
 Daly R. A., Sprinkle T. B., O’Dea C. P., Kharb P., Baum S. A., 2012, *MNRAS*, 423, 2498  
 Daly R. A., Stout D. A., Mysliwiec J. N., 2018, *ApJ*, 863, 117  
 Davis S. W., Laor A., 2011, *ApJ*, 728, 98  
 Dermer C., Finke J., Menon G., 2008, *Black-Hole Engine Kinematics, Flares from PKS2155-304, and Multiwavelength Blazar Analysis*. SISSA, Trieste  
 Dicken D. et al., 2014, *ApJ*, 788, 98  
 Fernandes C. A. C. et al., 2015, *MNRAS*, 447, 1184  
 Gallo E., Fender R. P., Miller-Jones J. C. A., Merloni A., Jonker P. G., Heinz S., Maccarone T. J., van der Klis M., 2006, *MNRAS*, 370, 13511360  
 Gelino D. M., Harrison T. E., Orosz J. E., 2001, *AJ*, 122, 2668  
 Gou L., McClintock J. E., Steiner J. F., Narayan R., Cantrell A. G., Bailyn C. D., 2010, *ApJ*, 718, L122  
 Grimes J. A., Rawlings S., Willott C. J., 2004, *MNRAS*, 349, 503  
 Heckman T. M., Best P. N., 2014, *ARA&A*, 52, 589  
 Heckman T. M., Kauffmann G., Brinchmann J., Charlot S., Tremonti C., White S. D. M., 2004, *ApJ*, 613, 109

- Ho L. C., 2009, *ApJ*, 699, 626  
 Jiang J. et al., 2019, *MNRAS*, 489, 3436  
 Jonker P., Nelemans G., 2004, *MNRAS*, 354, 355  
 Kuulkers E., Fender R. P., Spencer R. E., Davis R. J., Morison I., 1999, *MNRAS*, 306, 919  
 Lasota J. -P., 2000, *A&A*, 360, 575  
 McClintock J. E., Narayan R., Garcia M. R., Orosz J. A., Remillard R. A., Murray S. S., 2003, *ApJ*, 593, 435  
 McLure R. J., Willott C. J., Jarvis M. J., Rawlings S., Hill G. J., Mitchell E., Dunlop J. S., Wold M., 2004, *MNRAS*, 351, 347  
 McLure R. J., Jarvis M. J., Targett T. A., Dunlop J. S., Best P. N., 2006, *MNRAS*, 368, 1395  
 Meier D. L., 1999, *ApJ*, 522, 753  
 Merloni A., Heinz S., di Matteo T., 2003, *MNRAS*, 345, 1057  
 Mingo B., Hardcastle M. J., Croston J. H., Dicken D., Evans D. A., Morganti R., Tadhunter C., 2014, *MNRAS*, 440, 269  
 Narayan R., McClintock J. E., 2012, *MNRAS*, 419, L69  
 Netzer H., Trakhtenbrot B., 2014, *MNRAS*, 438, 672  
 Nisbet D. M., Best P. N., 2016, *MNRAS*, 455, 2551  
 O’Dea C. P., Saikia D. J., 2020, preprint ([arXiv:2009.02750](#))  
 O’Dea C. P., Daly R. A., Freeman K. A., Kharb P., Baum S., 2009, *A&A*, 494, 471  
 Owen F. N., Balonek T. J., Dickey J., Terzian Y., Gottesman S. T., 1976, *ApJ*, 203, L15  
 Raimundo S. I., Fabian A. C., Vasudevan R. V., Gandhi P., Wu J., 2012, *MNRAS*, 419, 2529  
 Rees M. J., 1984, *ARA&A*, 22, 471  
 Saikia P., Körding E., Falcke H., 2015, *MNRAS*, 450, 2317  
 Shahbaz T., Naylor T., Charles P. A., 1994, *MNRAS*, 268, 756  
 Shahbaz T., Bandyopadhyay R., Charles P. A., Naylor T., 1996, *MNRAS*, 282, 977  
 Shao Y., Li X.-D., 2020, *ApJ*, 898, 143  
 Skipper C. J., McHardy I. M., 2016, *MNRAS*, 458, 1696  
 Trakhtenbrot B., 2014, *ApJ*, 789, L9  
 Trakhtenbrot B., Volonteri M., Natarajan P., 2014, *ApJ*, 836, L1  
 Wu S., Lu Y., Zhang F., 2013, *MNRAS*, 436, 4271  
 Yuan F., Narayan R., 2014, *ARA&A*, 52, 529  
 Zdziarski A. A., Ziolkowski J., Mikołajewska J., 2019, *MNRAS*, 488, 1026  
 Ziolkowski J., Zdziarski A. A., 2018, *MNRAS*, 480, 1580  
 Zycki P. T., Done C., Smith D. A., 1999, *MNRAS*, 305, 231

## SUPPORTING INFORMATION

Supplementary data are available at [MNRAS](#) online.

**Table 6.** Mass accretion rates and efficiency factors for the NB16 LINERs.

Please note: Oxford University Press is not responsible for the content or functionality of any supporting materials supplied by the authors. Any queries (other than missing material) should be directed to the corresponding author for the article.

This paper has been typeset from a  $\text{\TeX}/\text{\LaTeX}$  file prepared by the author.